universität wien

MASTERARBEIT | MASTER'S THESIS

Titel | Title

Verification of the Accuracy of the Growth Rate Measurement Methodology at the CERN CLOUD Experiment

verfasst von | submitted by

Christian Sommer BSc

angestrebter akademischer Grad | in partial fulfilment of the requirements for the degree of

Master of Science (MSc)

Wien | Vienna, 2024

Studienkennzahl lt. Studienblatt | Degree programme code as it appears on the student record sheet:	UA 066 876
Studienrichtung lt. Studienblatt | Degree programme as it appears on the student record sheet:	Masterstudium Physics
Betreut von | Supervisor:	Assoz. Prof. Dr. Paul Winkler Privatdoz.

Acknowledgements

Greatest thanks to my supervisor Assoz. Prof. Dr. Paul Winkler for giving me the unique opportunity to participate in an international research campaign at CERN and to write my masters thesis about it. This project enabled me to gain insight into the work at what is probably the most important research centre in Europe.

Special thanks go out to Eva Sommer for her guidance at CERN and assistance throughout the writing process.

Furthermore, I would like to acknowledge the contributions of my colleagues of the aerosol group, who have offered their support and encouragement during challenging times.

I would also like to express my gratitude to my friends and companions, with whom I have shared countless adventures and precious memories. Their presence and contributions have perhaps made my university years the best time of my life.

Finally, the most significant acknowledgement is reserved for my parents and family. The love and support they have provided me with have allowed me to achieve everything I have.

Without the support of these individuals, this work would not have been possible. Thank you all for believing in me and being an integral part of this important milestone in my life.

Abstract

Atmospheric aerosols have a significant impact on the global climate system. Besides direct impacts of scattering and absorption on incoming solar radiation, increased aerosol number concentrations can lead to higher albedo and lifetime of clouds, inducing significant indirect radiative forcing. However, formation mechanisms as well as their interactions in the atmosphere are still poorly understood. Aerosols remain the main source of uncertainty for anthropogenic climate forcing.

The CLOUD (Cosmic Leaving Outdoor Droplets) experiment at CERN investigates the formation and growth of new atmospheric particles from reactive gases. In spring 2023 the technical run CLOUD16T was taking place, where in addition to baseline measurements a novel FLOw TUbe System (FLOTUS) was tested and characterised. Since wall losses in the CLOUD chamber limit the lifetime of aerosols, FLOTUS is designed as a chemical reactor to simulate aged trace gases in the atmosphere. These aged precursor vapours were then injected into the CLOUD chamber, where their nucleation potential, as well as their chemical composition was analysed.

In this thesis the obtained baseline measurements of growth rate were compared with results from previous CLOUD campaigns as well as with data from NAIS (Neutral Cluster and Air Ion Spectrometer) in order to verify the accuracy of the measurement methodology at the CLOUD project. For that purpose a DMA(Differential Mobility Analyzer)-train, especially developed for high-time resolution particle-size-distribution measurements below 10 nm was utilized.

The evaluation shows that the growth rates of DMA-train and NAIS are in line with expectations in the upper size range. However, comparisons with prior measurement campaigns indicate some differences in particle growth which might be caused by the installation of FLOTUS.

Zusammenfassung

Atmosphärische Aerosole haben einen bedeutenden Einfluss auf das globale Klimasystem. Neben direkten Auswirkungen auf die einfallende Sonnenstrahlung wie Streuung oder Absorption, können erhöhte Aerosolkonzentrationen zu einer höheren Albedo und Lebensdauer von Wolken führen, was einen erheblichen indirekten Strahlungsantrieb zur Folge hat. Jedoch werden Entstehung sowie Wechselwirkung von Aerosolen in der Atomosphäre nach wie vor nicht ausreichend verstanden und bilden weiterhin die größte Unsicherheit im Bereich des anthropogen verursachten Strahlungsantriebes.

CLOUD (Cosmic Leaving Outdoor Droplets) ist ein Projekt am CERN, das die Entstehung und das Wachstum neuer atmosphärischer Partikel aus reaktiven Gasen untersucht. Im Frühjahr 2023 fand die Forschungskampagne CLOUD16T statt, bei dem neben Basismessungen ein neuartiges FLOw TUbe System (FLOTUS) getestet und charakterisiert wurde. Da Wandverluste in der CLOUD-Kammer die Lebensdauer von Aerosolen begrenzen, ist FLOTUS als chemischer Reaktor konzipiert, um gealterte Spurengase in der Atmosphäre zu simulieren. Diese gealterten Gase wurden dann in die CLOUD-Kammer eingebracht, wo ihr Keimbildungspotenzial sowie ihre chemische Zusammensetzung untersucht wurden.

In dieser Arbeit wurden die aufgenommenen Basismessungen von Wachstumsraten mit Ergebnissen früherer CLOUD-Kampagnen sowie mit NAIS (Neutral Cluster and Air Ion Spectrometer)-Daten verglichen, um die Genauigkeit der Messmethodik von CLOUD zu überprüfen. Dafür wurde ein DMA (Differential Mobility Analyzer)-train verwendet, der speziell für Partikelgrößenverteilungsmessungen mit hoher Zeitauflösung unter 10 nm entwickelt wurde.

Die Auswertung zeigt, dass die gemessenen Wachstumsraten von DMA-train und NAIS im oberen Größenbereich den Erwartungen entsprechend übereinstimmen. Vergleiche mit früheren Messkampagnen weisen allerdings auf einige Unterschiede im Partikelwachstum hin, die unter anderem durch die Installation von FLOTUS erklärt werden könnten.

List of Abbreviations

AAN Advanced Aerosol Neutralizer.

CCN Cloud Condensation Nuclei.

CERN European Organization for Nuclear Research.

CI-APi-TOF Chemical Ionization Atmospheric Pressure interface Time-Of-Flight mass spectrometer.

CLOUD Cosmic Leaving Outdoor Droplets.

CPC Condensation Particle Counter.

DEG Diethylene Glycol.

DMA Differential Mobility Analyzer.

ELVOC Extremely Low Volatility Organic Compound.

FLOTUS Flow Tube System.

GCR Galactic Cosmic Rays.

GR Growth Rate.

HEPA High-Efficiency Particulate Air.

HOM Highly Oxygeneted Molecules.

HV High Voltage.

IVOC Intermediate Volatility Organic Compound.

LVOC Low Volatility Organic Compound.

MFC Mass Flow Controller.

NAIS Neutral Cluster and Air Ion Spectrometer.

nCNC nano Condensation Nucleus Counter.

NPF New Particle Formation.

PS Proton Synchroton.

PSM Particle Size Magnifier.

PTR3 Proton Transfer Reaction-Time-Of-Flight Mass Spectrometer.

SVOC Semivolatile Organic Compound.

TEI49C Thermo Environmental Instruments Model 49C.

VBS Volatility Basis Set.

VOC Volatile Organic Compound.

List of Symbols

$[ap]$	α-pinene concentration in cm^{-3}.
$[O_3]$	O_3 concentration in cm^{-3}.
α_c	condensation coefficient.
β	average growth rate.
η	gas viscosity.
λ	mean free path.
Φ	Fuchs correction factor.
ρ	density.
ρ_v	number density of condensable vapor.
σ	surface tension.
Θ	contact angle.
A	surface area of a droplet.
C	ozone concentration in ppm.
C_c	slip correction factor.
C^*	effective saturation concentration.
d_p	particle diameter.
D_v	diffusion coefficient of vapor.
E	electric field strength.
e	elementary unit of charge.
G	Gibbs free energy.
I	UV intensity in the sample gas.

i number of charges/molecules.

I_0 UV intensity in the reference gas.

J nucleation rate.

J_0 kinetic prefactor for the calculation of the nucleation rate.

$k(T)$ rate constant for the gas-phase reactions of O_3 with α-pinene.

K molecular absorption coefficient.

k Boltzmann constant.

L axial distance.

L^* length of the Model 49C cell.

$m(T, d_p)$ exponential relation coefficient for the gas-phase reactions of O_3 with α-pinene.

M molecular weight.

m contact parameter.

N_a Avogrado number.

p pressure.

p_∞ pressure far from the droplet's surface.

p_A partial pressure of a solute A.

p^S_A saturation vapor pressure of A in equilibrium with its liquid phase.

Q_a aerosol flow rate.

Q_{ex} excess air flow.

Q_{sh} sheath air flow.

Q_s sample air flow.

R ideal gas constant.

r radius of a particle.

R_i surface radius and radii of electrodes.

r^* Kelvin radius.

S saturation ratio.

T temperature.

t time.

V voltage.

v velocity.

v_{l} volume occupied by a molecule in the liquid phase.

Z electric mobility.

Z^* Zeldovich nonequilibrium factor.

Contents

1 Introduction

Aerosols are defined as a mixture of microscopically small, solid or liquid particles suspended in a gas. They are two-phase systems which consist of both the particles and the carrier gas in which they are suspended. If particles are emitted directly into the atmosphere, the resulting aerosol is referred to as a primary aerosol. Secondary aerosols are composed of particles which are produced in the atmosphere by chemical reactions of gaseous compounds [1]. Additionally, aerosols can be distinguished according to whether they are of anthropogenic or natural origin. The major part of the atmospheric aerosol is made up of organics as well as inorganic substances, mineral species, black carbon and primary biological aerosol particles. While constituents such as sulphate, mineral dust and ammonium for instance are mainly of anthropogenic origin, primary biological aerosol particles, mineral dust and sea salt are classically of natural production [2]. Important phenomena which are caused by aerosols are dust, fume, smoke, mist, haze, fog or most importantly clouds [1].

Aerosols play a significant role in the Earth's energy balance by scattering and absorbing sunlight and radiation. Especially the enhanced concentration of human-made atmospheric aerosols leads to a crucial impact. They affect properties and lifetime of clouds as well as emissions of natural aerosols, hence they are contributing to a change in the Earth's climate system [3]. Furthermore, certain particulate air pollutants may cause severe health issues as well as environmental problems leading to premature deaths, smog or acid deposition to name just a few examples [4].

Atmospheric aerosols are produced not only by direct emissions from sources

like combustion processes, volcanoes, or sea spray but also in the atmosphere from condensable vapors via a process known as New Particle Formation (NPF) [5]. The primary source of Cloud Condensation Nuclei (CCN) in nature is NPF by gas-to-particle conversion. The survival chance of newly formed particles and therefore their climatic significance is especially determined by the early steps of particle growth between 1 and 10 nm [6]. NPF can be understood as a two-phase process: in the first stage thermodynamically stable clusters (in the size range of around 1 nm [7]) are formed by homogeneous nucleation, while in the second stage the clusters grow through condensation and coagulation into quasi-stable aerosol particles (typically $d_p > 3$ nm). If the growth is not sufficiently fast, the clusters coagulate with the pre-existing aerosol population and are removed, resulting in no New Particle Formation [8]. In simple words, gas molecules collide and stick to each other to create new atmospheric aerosol particles [9].

Furthermore, the presence of ions plays a significant role in NPF. They enhance the stability of freshly formed molecular clusters and reduce their evaporation rates, leading to increased particle formation [10].

The mechanism of NPF occurs almost everywhere in the troposphere and has been observed both in natural environments as well as in areas with heavy anthorpogenic influence such as mega cities [11]. About 50 % of the global CCN are estimated to originate from NPF [8]. With few exceptions, NPF primarily occurs during the daytime, often as an outburst of new particles around midday [12]. This suggests the significance of photochemistry in some stages of the formation process. Further conditions to increase NPF are low condensation sink, low relative humidity and high vapor source rate [11].

New Particle Formation events can be identified by the sudden emergence of a new mode showing high concentrations of particles on the smallest nano scale. The characteristic pattern of a NPF event on a logarithmic plot is commonly known as a "banana plot" [13]. An example illustration is shown

in Figure 1. The Figure presents a simulation from publication [14]. It also includes the corresponding particle formation rate. Major physical quantities to describe the phenomenon NPF are, on the one hand, the nucleation rate J and, of greater importance for the present work, the growth rate GR [7].

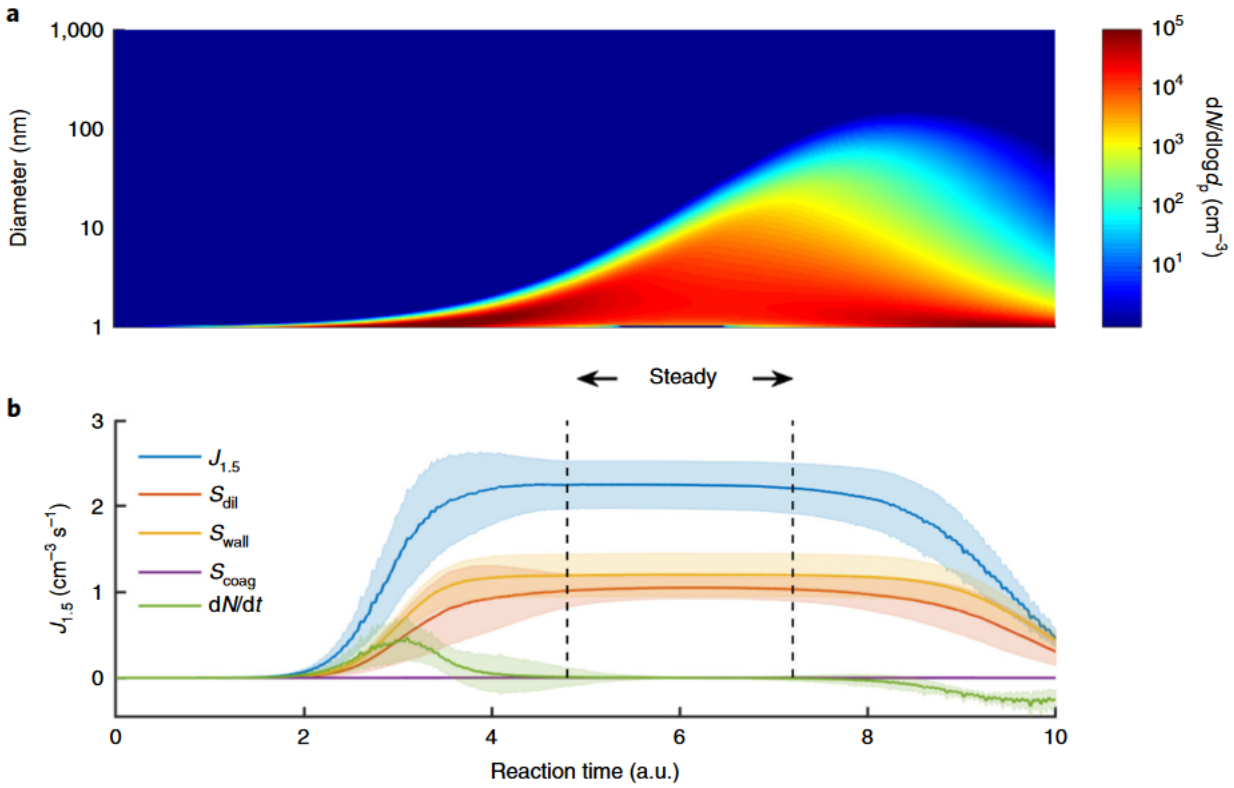

Figure 1: a, example of a simulated logarithmic "banana plot" taken from [14]: The red areas represent high concentrations of particles, the blue areas represent low particle concentrations. b, corresponding particle formation rate

The primary vapors responsible for particle growth include sulfuric acid and perhaps of greater significance, low-volatility organic compounds produced by the oxidation of volatile organic compounds (VOCs) [6].

In urban areas large amounts of VOCs are emitted in combustion processes, mainly by vehicles. However, studies pointed out that VOC emissions by plants are at least of the same importance. Isoprene (C_5H_8) and monoterpenes ($C_{10}H_{16}$) are the most significant atmospheric biogenic VOCs with α-pinene being the most abundant. Primary oxidation of VOCs by O_3, $OH\cdot$ or NO_x is often followed by a auto-oxidation process which can develop highly

oxygenated molecules (HOMs). Recent publications indicate that those substances are also capable to form and grow particles and therefore influence atmospheric NPF [7].

In summary, aerosols play an important role both in nature and in society, which is why it is extremely important to investigate their formation pathways and dynamics on a fundamental level.

α-pinene ozonolysis investigations can be performed at the CERN CLOUD experiment [7]. The intention of the CLOUD experiment is to study the microphysics of the interactions between galactic cosmic rays and clouds. However, clouds are barely generated in the chamber, rather NPF is investigated and the experiments terminate when particles reach a diameter of ~ 100 nm. The investigations take place in a controlled laboratory setting where the experimental parameters can be precisely controlled and measured [15]. For that purpose a large chamber is used, where its contents are continuously sampled and analysed by a variety of instruments. It is a unique laboratory experiment designed to characterize the full parameter space in the gas and particle phase. Among others, nucleation and growth rate are the most important quantities with respect to the particle phase [16].

The aim of this master's thesis is to compare baseline measurements of particle growth rates obtained in the technical campaign CLOUD16T with measurement results from CLOUD15, as well as with data from NAIS (Neutral Cluster and Air Ion Spectrometer) and published literature values from CLOUD12 in order to verify the accuracy of the growth rate measurement methodology at the CERN CLOUD experiment. For that purpose a DMA(Differential Mobility Analyzer)-train, especially developed for high-time resolution particle-size-distribution measurements below 10 nm, is utilized.

2 | The CERN CLOUD Experiment

The following chapter introduces the CERN CLOUD experiment and the CLOUD16T campaign in particular.

The CLOUD experiment consists of an international research team of scientists from 17 universities in nine countries with the purpose to investigate the possible link between cosmic rays and the formation of clouds. A first pilot experiment was carried out during a four-week run in fall 2006 [17]. Centerpiece of the experiment is a 26.1 m^3, electropolished, stainless-steel aerosol chamber that makes it possible to conduct New Particle Formation experiments under different ionization levels. Figure 2 illustrates the setup of the measuring container schematically and names all important components.

At the top and bottom of the chamber, covers with a diameter of 1 m are located to enable internal access. The chamber is equipped with several ports to allow the installation of electrical or optical transmission lines as well as sampling probes for extracting air samples. Inside the vessel two electrodes, capable of operating at voltages up to 30 kV, are installed to create an ion-free environment. However, the chamber's contents can also be irradiated with UV light in a wavelength range of 250-400 nm. The UV light is provided by vacuum fibre optics to ensure a consistent UV irradiation inside for photolytic reactions, without introducing any unwanted heat stress. All materials and procedures used for the chamber are carefully selected to minimize the presence of contaminant vapors [18]. Chamber and gas system are designed to operate at 5 mbar above atmospheric pressure (1013.25 mbar), in order to prevent contamination by unwanted gases. For experiments involving the

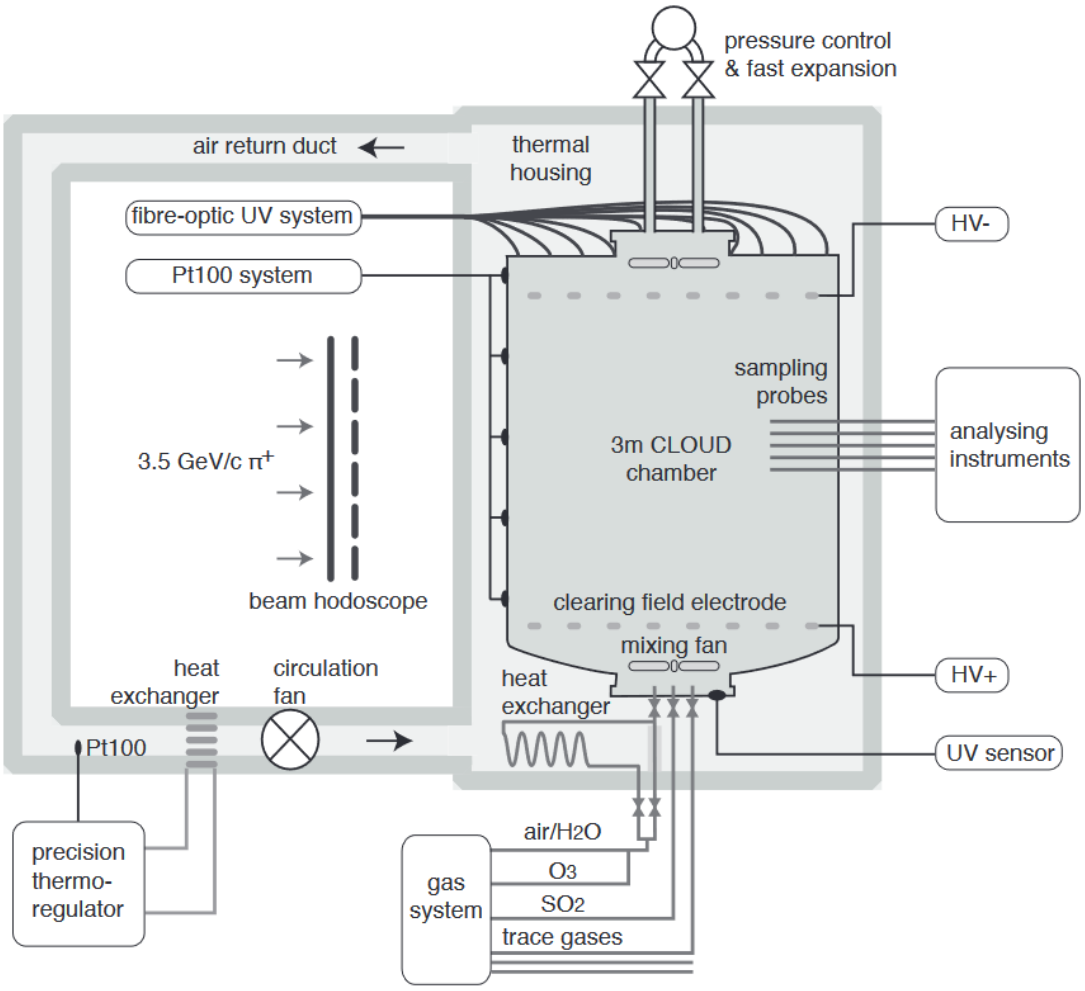

Figure 2: Schematic of the CLOUD chamber at CERN [18].

formation of real clouds, however, the chamber is briefly brought to over 200 mbar above and down to 65 mbar below atmospheric pressure [19]. The vessel is encased by an insulated thermal housing to keep the internal temperature constant. Experiments can be conducted at highly stable temperatures, with precision down to approximately 0.01°C, ranging from 40°C to -70°C. Furthermore, the CLOUD chamber is capable of being raised to a temperature of 100°C for the purpose of bakeout. Importantly, the chamber can be exposed to a pion beam from the CERN Proton Synchroton (PS) to simulate ion production rates in the upper troposphere. Ultra-pure synthetic air is produced by evaporating cryogenic liquid nitrogen (N_2) and liquid oxygen (O_2), mixed in a 79:21 ratio, respectively. The resulting air is then humidified using ultra-pure water sourced from a filtered recirculation system. Ozone (O_3) is added by UV irradiation. Further trace gases such as SO_2, NH_3, α-pinene ($C_{10}H_{16}$) or

pinanediol ($C_{10}H_{18}O_2$) can be injected very accurately by separate inlet lines. Stainless steel fans are installed in order to mix the fresh gases and beam-ions to ensure homogenity inside the vessel [18].

The CLOUD chamber is operated and monitored in the so-called 'control room', which is located directly next to it. A large set of computers and monitors allow complete observation of all the processes inside the chamber.

The condensation sink for CLOUD, also referred to as the wall loss rate, is $2.2 \cdot 10^{-3} s^{-1}$, which corresponds to the Pristine Boundary Layer [20]. To compensate for sampling losses, fresh gas flows continuously into the container at a rate of up to 140 liters per minute, which leads to a dilution lifetime of approximately 3 hours [18].

Figure 3: Photography of the CLOUD container during the CLOUD16T measurement campaign (©Christian Sommer).

2.1 The CLOUD16T Measurement Campaign

Between April 17th and May 12th 2023 the technical run CLOUD16T ("T" signifies "technical") was taking place at CERN. Main objective of the campaign was to test and characterize a newly installed FLOw TUbe System (FLOTUS).

CLOUD is limited to investigating rapid gas phase oxidation of organic precursor vapors within approximately one hour, since wall losses decrease the lifetime of particles and vapors. Therefore CLOUD cannot observe a wide range of oxidation processes that take place in the real atmosphere over extended timescales involving repeated independent oxidation steps [16].

FLOTUS is designed as a chemical reactor to mimic the aging of organic trace gases in the atmosphere. Trace gases are permanently exposed to chemical reactions that change their properties over time. This occurs mainly through hydroxyl radicals (OH), which interact with the gas molecules. FLOTUS is made up of a 3 m long quartz tube with an inner diameter of 20 cm, surrounded by a set of high intensity UV lamps. When the mixture of trace gases, ozone and water vapor passes the pipe, the UV lamps produce high levels of OH radicals, which then react with the gas system. The outflow, oxidized organic precursor vapors, will then be fed into the CLOUD chamber where the chemical composition as well as the nucleation potential of those "aged" vapors can be studied [21]. A schematic is provided in Figure 4.

As in regular CLOUD runs the content of the chamber was closely monitored by various instruments analysing the chemical and physical properties of the gas phase, clusters and aerosol particles. The major tasks of CLOUD16T were to investigate flow conditions and reaction times in FLOTUS as well as the transmission efficiency of the vapors into the CLOUD chamber. A standard experiment usually begins with the injection of α-pinene into a neutral (ion free) chamber environment. The ozone already present reacts immediately with the α-pinene and starts to form aerosol particles [12]. The DMA-train as

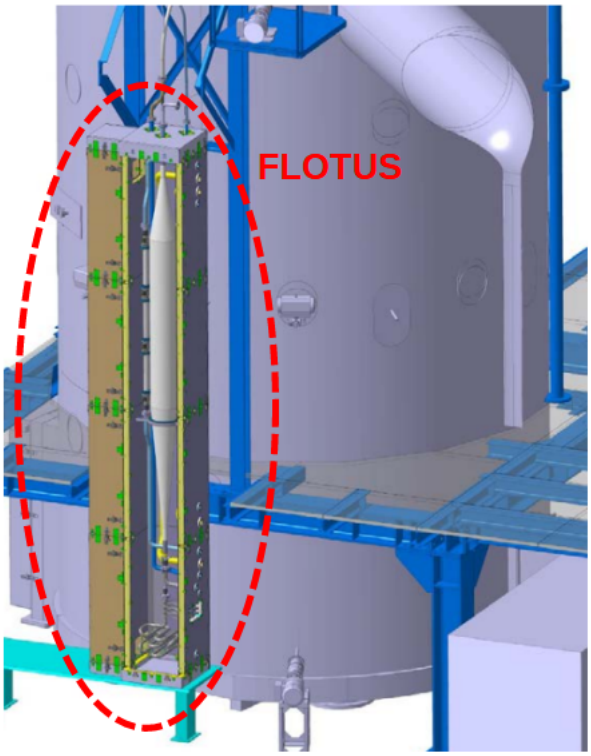

Figure 4: FLOTUS at CLOUD (highlighted): a 3 m long laminar-flow quartz drift tube designed for exposing organics and other vapors to hydroxyl radicals simulating the chemical transformation of precursor gases in the real atmosphere over the course of several days. The output is led into the CLOUD chamber for investigations of "aged" organic compounds. All operational parameters are controlled separately from the CLOUD chamber. Schematic adapted from [16].

one of those instruments helped to analyse the particle formation potential in the chamber. Furthermore, three baseline measurements were conducted, one each in GCR (galactic cosmic rays), beam and neutral mode. These baseline measurements serve as a reference for comparison in order to assess the impact or effectiveness of the measures. GCR is considered to be a stage in which neither an electric field nor the PS beam is in operation. This means that there occurs a natural ion background like in the atmosphere at ground level. In the beam stage, the beam of the PS is turned on, simulating conditions in the upper free troposphere resulting in a higher number concentration of ions. In neutral stage, the electric field is active, filtering out all charges in the chamber at a time scale of a few seconds.

Operation and monitoring of the CLOUD chamber and FLOTUS during CLOUD16T was carried out in three equally long shifts per day, during which

the operators - two persons each - in the control room conducted the measurement spanning the entire campaign. The tasks of the shift operators were the implementation of the daily updated operating plan as well as performing the cleanings of the chamber that occurred between the stages. The run plan was discussed daily at 3 p.m. by the whole team. The shifts covered the following time slots:

1. shift: from 7 a.m. to 3 p.m.
2. shift: from 3 p.m. to 11 p.m.
3. shift: from 11 p.m. to 7 a.m.

In addition to the shift duties in the control room, my major task was to operate and maintain the DMA-train. That includes for instance measuring flows, refilling working fluids or keeping the logbook up to date. Related incidents will be addressed in a later chapter.

3 | Theory and Concepts

For a complete understanding of the experiment's setup and data analysis, the physical backgrounds are crucial. These will be explained more detailed in the following chapter.

3.1 Nucleation

Nucleation is the first step in the phase transformation from vapor to liquid (condensation). Liquid does not occur instantly, rather small nuclei must form initially in the gas phase. The process of nucleation can occur in the absence and presence of foreign material. The two main types of nucleation are described in the next sections.

3.1.1 Homogeneous Nucleation

The formation of particles without the assistance of condensation nuclei or ions is called homogeneous nucleation [1]. This process occurs in a supersaturated vapor phase. The degree of supersaturation of a solute in air at a certain temperature T is determined by the saturation ratio:

$$S = p_{\mathrm{A}}/p^{\mathrm{s}}{}_{\mathrm{A}}(T) \tag{3.1}$$

In this formula p_A refers to the partial pressure of the solute A and $p^s{}_A(T)$ the saturation vapor pressure of A in equilibrium with its liquid phase at temperature T. There are three different cases:

1. S<1 for subsaturated vapor
2. S=1 for saturated vapor

3. S>1 for supersaturated vapor

Isothermal compression, isobaric cooling and adiabatic expansion for instance, are processes to bring an unsaturated or saturated vapor into a state of supersaturation.

Equation 3.2 is an expression for the Gibbs free energy. It describes the energy necessary to form a cluster with i molecules. According to [13], the equation is given by:

$$\Delta G_{\mathrm{i}} = 4\pi\sigma {r_{\mathrm{i}}}^2 - \frac{4\pi}{3}\frac{kT\ln S}{v_{\mathrm{l}}}{r_{\mathrm{i}}}^3 \tag{3.2}$$

Here r_i marks the radius of the formed cluster, σ the surface tension and v_l the volume occupied by a molecule in the liquid phase. T denotes the temperature, k the Boltzmann factor. The formula contains of two terms. The first one refers to the surface, the second to the volume of the cluster. The surface term always remains positive, while the volume term becomes negative when S>1. Thus, at subsaturation the free energy increases with increasing radii. The free energy of a supersaturated vapor, however, grows until the volume term overtakes the surface term. At a certain critical radius r^*, the Gibbs free energy reaches a maximum. The corresponding radius r^*, the so-called Kelvin radius, can be calculated by deriving ΔG_i by $d(r_i)$ and setting equal 0:

$$r^* = \frac{2\sigma v_{\mathrm{l}}}{kT\ln S} \tag{3.3}$$

By substituting equation 3.3 into equation 3.2 the free energy barrier height is defined:

$$\Delta G^* = \frac{4\pi}{3}\sigma {r^*}^2 = \frac{16\pi}{3}\frac{{v_{\mathrm{l}}}^2\sigma^3}{(kT\ln S)^2} \tag{3.4}$$

Using the saturation ratio and equation 3.3, the Kelvin equation can be ex-

pressed:

$$S = p_{\mathrm{A}}/p^{\mathrm{s}}{}_{\mathrm{A}}(T) = \exp\left\{\frac{2\sigma v_{\mathrm{l}}}{kTr^*}\right\} \tag{3.5}$$

When the partial pressure of vapor at the droplet surface is p_a, the radius r^* is the size at which the droplet neither grows nor evaporates. The Kelvin equation defines a specific ratio, the Kelvin ratio, that enables mass equilibrium for a given particle size r^*. That means for a specific Kelvin ratio droplets with a radius r^* are stable, larger ones grow and smaller ones evaporate. Since the exponent on the right hand side of the equation is always positive, thus equilibrium can only be reached when S>1. Moreover the Kelvin equation displays that the saturation ratio over a curved surface is always higher than over a plane surface. The surface curvature slightly modifies the attractive forces between the surface molecules, making it easier for molecules to escape the droplet surface. To maintain mass equilibrium and prevent this evaporation, the partial pressure of vapor surrounding the droplet must exceed $p^s_A(T)$ [13].

3.1.2 Heterogeneous Nucleation

The process of heterogeneous nucleation involves the presence of a foreign substance or surface, such as an ion or a solid particle [13]. In comparison to homogeneous nucleation, which usually requires saturation ratios exceeding several hundred percent, heterogeneous nucleation starts to occur at supersaturations of a few percent. Heterogeneous nucleation is primarily responsible for the formation of clouds in the atmosphere. There are three types of nuclei: insoluble nuclei, soluble nuclei and ions [1].

Insoluble Flat Foreign Surface

Insoluble nuclei can act as passive sites for the condensation of supersaturated vapor. At supersaturation, an insoluble nucleus with a wettable surface is covered with an adsorbed layer of vapor molecules [1]. The (cluster) formation

free energy on a flat solid surface can be written as [13]:

$$\Delta G^*_{\text{het}} = \Delta G^*_{\text{hom}} f(m) \tag{3.6}$$

where ΔG^*_{hom} is the nucleation work for homogeneous critical nucleus formation and m is the contact parameter, that connects the contact angle Θ between the nucleus and the substrate as well as the interfacial tensions between the different phases.

$$m = \cos\Theta = \frac{\sigma_{\text{SV}} - \sigma_{\text{SL}}}{\sigma_{\text{LV}}} \tag{3.7}$$

with σ representing the interfacial tensions between the different phases, subscript V denotes the gas phase, L the nucleus and S the substrate. The function f(m) is then composed as follows:

$$f(m) = \frac{1}{4}(2+m)(1-m)^2 \tag{3.8}$$

The function approves values between 0 and 1. When the contact angle Θ yields 0, m=1 and f(m)=0. At this point nucleation begins as soon as the equilibrium saturation ratio is exceeded, since the free-energy barrier is zero. In the opposite case, when $\Theta = 180$ and f(m)=1, heterogeneous nucleation is not favored over homogeneous nucleation [13].

Insoluble Spherical Foreign Surface

In case of a spherical surface, beside the contact angle the relation between the critical embryo radius and the seed particle radius is of importance. The free energy ΔG^* to form an embryo of critical radius r^* on a curved surface of radius R is given by:

$$\Delta G^* = \Delta G^*_{\text{hom}} f(m,x) \quad \text{with} \quad x = \frac{R}{r^*} \tag{3.9}$$

The function f(m,x) incorporates the geometry of the particle and results as:

$$f(m,x) = \frac{1}{2}\left\{1 + \left(\frac{1-mx}{g}\right)^3 + x^3\left[2 - 3\left(\frac{x-m}{g}\right) + \left(\frac{x-m}{g}\right)^3\right] + 3mx^3\left(\frac{x-m}{g} - 1\right)\right\} \tag{3.10}$$

with

$$g = \left(1 + x^2 - 2mx\right)^{1/2} \tag{3.11}$$

The function f(m,x) varies between 1 and 0, based on the contact parameter m and the relative size x of foreign particles. It basically describes the quantity of the reduction of the nucleation barrier [22]. This means that the smaller a particle, the better it is suited for nucleation. Furthermore, insoluble particles with small contact angles are ideal for nucleation, while particles with large contact angles do not support nucleation. [13].

Nucleation on Soluble Nuclei

Nucleation on soluble substances is the major formation process of water droplets in nature, with sodium chloride being the most important soluble nucleating material. Sodium chloride nuclei are present across the whole atmosphere, since they are formed in large numbers in the oceans. The salt dissolved in the water decreases the equilibrium vapor pressure above the water surface. This effect enables particle growth at a lower degree of saturation than with pure water. Only supersaturations of a few percent are required. Soluble nuclei are the reason why supersaturations barely exceed those few percent. The formation of particles on soluble nuclei uses all the available excess vapor and thus avoids other mechanisms from becoming active [1].

Ion-induced Nucleation

Earth's atmosphere contains around 1000 ions cm^{-3}, which are produced either by cosmic radiation or radioactive gases. Ions are single-charged and, more importantly, stable clusters which promote nucleation at supersaturations above 2.0. However, since our atmosphere is full of condensation nuclei, which can induce nucleation at much lower levels of supersaturation, the effect of ions can be considered as negligible [1].

3.1.3 Nucleation rate

The nucleation rate J is defined as the net rate at which critical clusters are created [23]. According to [11] the nucleation rate can be represented as:

$$J = J_0 \exp\left\{-\frac{\Delta G^*}{k_\mathrm{B} T}\right\} \tag{3.12}$$

with J_0 being a kinetic prefactor and ΔG^* the free energy of formation. J_0 is dependent on the surface area A of a droplet, the average growth rate β, the Zeldovich nonequilibrium factor Z^* and the number density of the condensable vapor ρ_v:

$$J_0 = A\beta Z^* \rho_\mathrm{v} \tag{3.13}$$

3.2 Condensation and Particle Growth Rate

As soon as a stable particle is created, which is characterized by exceeding the diameter d^* at a certain saturation ratio, the particle starts to grow by condensation [1]. In atmospheric science and aerosol physics the Particle Growth Rate (GR) refers to the rate of change in particle diameter, typically due to processes like condensation, evaporation and coagulation. GRs are essential to characterize particle formation in the atmosphere. The quantity is defined as:

$$GR = \frac{\mathrm{d}d_\mathrm{p}}{\mathrm{d}t} \tag{3.14}$$

with d_p representing the particle diameter [14] and is usually expressed in [nmh^{-1}].

As stated in [1], the rate of growth depends on three variables: the size of particles, their relation to the gas mean free path and the relative humidity. Initially, when a particle begins to grow, its dimensions are typically smaller than the mean free path λ and hence the particle growth rate is determined by the rate of random molecular impacts between particle and vapor molecules. In this case GR is given by the following expression:

$$\frac{\mathrm{d}d_p}{\mathrm{d}t} = \frac{2M\alpha_c(p_\infty - p_d)}{\rho_p N_a \sqrt{2\pi m k T}} \quad \text{for} \quad d_p < \lambda \tag{3.15}$$

where M is the molecular weight of the liquid, α_c the condensation coefficient, p_∞ the pressure far from the droplet's surface, p_d the partial pressure at droplet surface, ρ_p gives the density of the liquid, N_a the Avogrado number and m the mass of the vapor molecule [1].

When the particles then grow larger than the mean free path, GR no longer depends on the random molecular collision rate, but on the rate at which vapor molecules diffuse to the surface of the particle. The rate of increase of the particle diameter can then be written as:

$$\frac{\mathrm{d}d_p}{\mathrm{d}t} = \frac{4D_v M}{R\rho_p d_p}\left(\frac{p_\infty}{T_\infty} - \frac{p_d}{T_d}\right)\Phi \quad \text{for} \quad d_p > \lambda \tag{3.16}$$

Here D_v denotes the diffusion coefficient of the vapor, R the ideal gas constant, T_∞ the temperature away from the droplet surface, T_d the temperature at the droplet surface and Φ is the Fuchs correction factor [1]. The equation is derived from the theory of molecular diffusion at the droplet surface, which becomes invalid for distances shorter than the mean free path of the gas from the particle surface. To correct for this effect, the Fuchs factor is introduced [11].

3.2.1 Experimental Determination of Growth Rates: Appearance Time Method

During a particle formation event for instance in the CLOUD chamber, the GR is generally determined by measuring the time evolution of the particle number size distribution. There are several methods to perform this. In this work the so-called "Appearance Time Method" is applied to identify particle growth rates. This approach relies on figuring out when new particles of a specific size first show up, and then calculating the growth rate by looking at how much time passes between different sizes [24]. Here the principle of the appearance time method is outlined:

1. Determination of the appearance time $t_{\text{app50,i}}$, which is the time when the concentration in size bin i meets 50% of its maximum. This is performed by fitting a Sigmoid function to the concentration time series.
2. Graph the mean diameters of the size bins, $t_{\text{p,mean,i}}$, against their respective appearance times $t_{\text{app50,i}}$.
3. Perform a linear regression on the size range that determines the GR.
4. Calculate the GR as the slope of the linear fit [14].

During the CLOUD16T campaign GRs over two different size intervals were obtained: [1.8-3.2] nm and [3.2-8.0] nm. The advantages of this measurement method include robust GRs for chamber experiments. Additionally, the results remain unaffected by significant uncertainties in absolute particle concentrations due to potential evaporation effects [6].

3.3 Highly Oxygenated Molecules and Volatile Organic Compounds

In this section the terms HOM and VOC are briefly explained and how molecules can be classified accordingly.

3.3.1 Highly Oxygenated Molecules (HOM)

HOM are a recently found group of compounds. According to [25] there is a set of criteria to classify molecules as HOM:

1. HOM are produced by autoxidation. The process of autoxidation describes how a peroxy radical forms a hydroperoxide functionality and an alkyl radical by undergoing an intramolecular hydrogen-atom shift. Subsequently, molecular oxygen quickly attaches to create a new, more oxidized peroxy radical. In comparison to other compounds with similar elemental composition HOM include at least one, mostly multiple hydroperoxide, peroxide, or peroxy acid groups.

2. HOM are formed in the gas phase under atmospheric conditions. Since autoxidation is also an important effect in liquid-phase and combustion processes, the term HOM is specifically used for compounds produced under atmospherically relevant conditions.

3. HOM consist of six or more oxygen atoms. The limit of six is more an artificial criterion, since there exist cases of compounds containing less than six O atoms which may be characterized as HOM. However, at six oxygen atoms molecules are very likely to have already undergone autoxidation.

α-pinene reacts with O_3 to form oxidation products such as HOMs. α-pinene ozonolysis is an important form of autoxidation. A comprehensive understanding of the products and pathways of this mechanism is important for modelling atmospheric chemistry and predicting aerosol formation. It serves as a well characterized test system in CLOUD.

3.3.2 Volatility Classes

Another way to classify molecules is based on their volatility. The volatility of a substance is referred to as a measure, how likely the substance transfers from the liquid or solid phase to the vapor phase. Under fixed temperature and pressure conditions, a substance with high volatility rather exists as a vapor

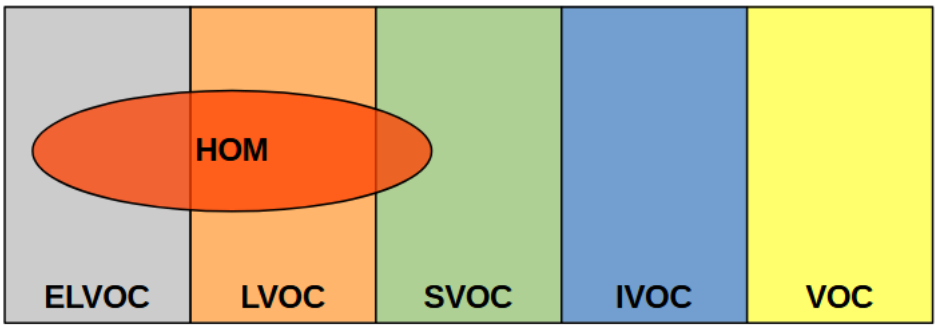

Figure 5: Euler diagram, not to scale, illustrating the relation between HOM and the different volatility classes. The position of HOM in the diagram is approximated using commonly published elemental formulas of HOM and their volatility estimates. HOM are mainly ELVOC or LVOC, even though some might be volatile enough to be classified as SVOC. Based on [25].

than a substance with low volatility, which prefers the liquid or solid state [26].

Labelled as Volatility Classes, five groups are suggested, which are distinguished according to their effective saturation concentration C^*. Saturation concentration and volatility can be used synonymously and the unit of C^* is μgm^{-3} [27].

The grouping according to [25]:

1. Extremely Low Volatility Organic Compounds (ELVOC): $C^* < 3{\cdot}10^{-5}\mu gm^{-3}$
   Molecules of this group can condense onto almost every pre-existing cluster. Together with other ELVOCs, they can directly participate in NPF processes.

2. Low Volatility Organic Compounds (LVOC): $3 \cdot 10^{-5} < C^* < 0.3\mu gm^{-3}$
   These molecules condense onto particles that exceed a certain size limit. They might not condense onto the smallest particles due to the Kelvin effect.

3. Semi-volatile Organic Compounds (SVOC): $0.3 < C^* < 300\mu gm^{-3}$
   At atmospheric equilibrium conditions these molecules are able to exist in relevant fractions in the condensed phase as well as in the vapor phase.

4. Intermediate Volatility Organic Compounds (IVOC): $300 < C^* < 3 \cdot 10^6 \mu g m^{-3}$
   Molecules almost exclusively existing in the gas phase.

5. Volatile Organic Compounds (VOC): $C^* > 3 \cdot 10^6 \mu g m^{-3}$
   These molecules are identified as volatile in all situations and play a dominant role in gas-phase oxidation chemistry in the atmosphere.

Figure 5 provides a graphic illustration of the relationship between HOM and VOC.

Experimental and model studies have demonstrated that HOMs resulting from α-pinene ozonolysis can be categorized as SVOC, LVOC, and ELVOC [28]. Organic compounds that contain many oxygen molecules, meaning they are highly oxidised, can condense very well. In addition, substances with low volatility are also easily condensable. This indicates that condensable VOCs are just another classification for HOMs.

Since the volatilities of organic compounds in the atmosphere vary greatly (>10 orders of magnitude), it is often easier to simplify the process of gas-to-particle partitioning by grouping similar compounds together in a volatility basis set (VBS) [6]. Typically, compounds are sorted in bins based on their mass-equivalent effective saturation concentration (C^*), which is represented using a logarithmic distributed basis set [29].

4 Instrumentation

The centrepiece of this work is the DMA-train. This chapter introduces the functionality of the DMA-train, followed by a detailed description of its individual components. Furthermore, those instruments are explained, which were not directly operated by myself but provide necessary information for the data evaluation in the next chapter.

4.1 The DMA-train

The Differential Mobility Analyzer train (DMA-train) was developed at the University of Vienna and is used to obtain fast and precise size-distribution measurements in the sub-10 nm range. This method is particularly useful for rapidly changing aerosol, such as New Particle Formation during nucleation events. One of the DMA-train's key benefits is its ability to detect aerosol particles smaller than 2.5 nm, which sets it apart from other measurement devices using the same principle. Basically, the DMA-train is designed for measurements in a size range of approximately 1.8 to 10 nm and sensitive to low particle number concentrations. It consists of six Differential Mobility Analyzers (DMA) operating in parallel. Each DMA operates at different fixed voltages, resulting in different particle sizes. Furthermore, one Particle Size Magnifier (PSM), one Nano-Enhancer - both used for channels below 2.5 nm - and six state-of-the-art Condensation Particle Counters (CPC) are attached [30].

The DMA-train was constructed in a symmetrical two layered design, both layers consisting of three DMAs. This design was chosen to keep the instrument as compact as possible. Within the mounted and fixed setup, all

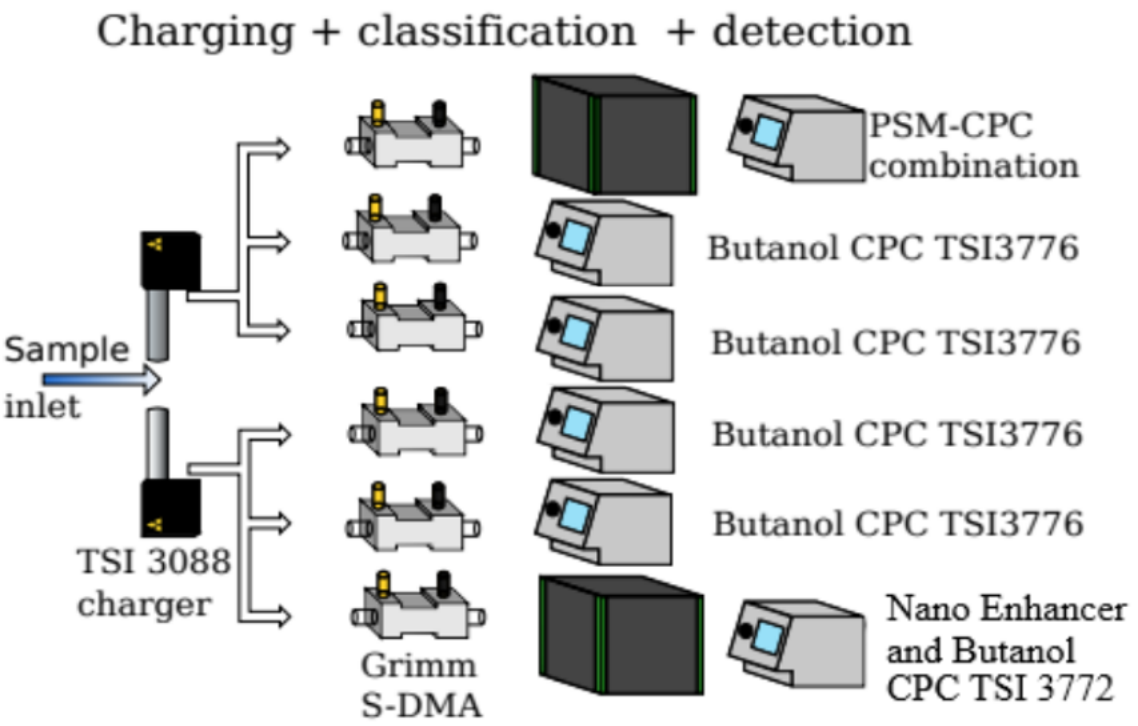

Figure 6: Schematic setup of the DMA-train: The sample flow coming from the left is first split between the two levels and charged by the AANs. For classification, the two separate flows are parted again and pass through the DMAs. Detection by the particle counters takes place in the last section. Figure modified from [30].

necessary devices such as power supplies, flow pumps and controls plus a uniform data acquisition system are provided. The flow pipe system is assembled identically in length and shape. This guarantees equal flow patterns and avoids high particle concentration losses due to diffusion. The inlet of the DMA-train is located between the two levels of the DMA-train. The combined sample flows of the used CPCs provide a common flow of 11 $lmin^{-1}$ for all channels. In order to minimize further diffusion losses, a make-up flow of 9 $lmin^{-1}$ in the main sampling line is added by the sample flow and controlled by a critical orifice.

A 0.5 inch T-piece is used to split up the incoming flow into two transport flows with 5.5 $lmin^{-1}$ for each level. The design of the DMA-train resembles the standard approach of a differential/scanning mobility particle sizer, depicted in Figure 6.

Both flows pass through a TSI Inc. model 3088 Advanced Aerosol Neutralizer (AAN), a soft X-ray bipolar diffusion charger. [31] stated that, even at high flow rates of up to 16 $lmin^{-1}$, the size distribution of negatively charged aerosol particles does not exceed mobility diameters of 1.6 mm. Thus, a lower sizing limit of the DMA-train is defined.

After the AAN, the aerosol achieves a defined charging state and is parted into two 1.5 $lmin^{-1}$ and one 2.5 $lmin^{-1}$ stream by a three-way flow splitter on each level. The aerosol is then classified in six "Vienna-type" S-DMAs, which are operated at a sheath air flow rate of 15 $lmin^{-1}$. A single high throughput vacuum pump with eight distinct pumping chambers regulated by temperature controlled critical orifices provides the sheath air. The radii of the identical DMAs are: R_i = 0.013 m and R_o = 0.020 m (inner and outer radius). At particle diameters above 5 nm better counting statistics make it possible to set one DMA to alternate every 10 s between 6.2 nm and 8.0 nm. This results in a total of seven measured sizes for the DMA-train [6], which are depicted together with their corresponding voltages in the following Table 1.

Detector	PSM	Nano-Enhancer	CPC 1	CPC 2	CPC 3	CPC 4	CPC 4
Size channel (in nm)	1.8	2.2	2.5	3.2	4.3	6.2	8.0
DMA voltage (in V)	22	31	41	63	116	227	375

Table 1: Channels and corresponding voltages of the DMA-train.

HEPA filters and active charcoal filters clear the sheath air circuits from remaining aerosol particles and chemical contaminations. Six equal 2.26 l silica-gel dryers are attached to keep the sheath air dry. The pumping circuits are monitored by sensors for temperature, pressure and relative humidity. Furthermore the central electrode of the S-DMAs can receive positive voltages up to +6 kV from six identical HV modules manufactured by Grimm Aerosol Technik GmbH & Co.

The detection is the next step following the classification, performed by six state of the art Condensation Particle Counters. For this purpose four chan-

nels use TSI 3776 butanol-based ultrafine CPCs with a corresponding cutoff diameter as low as around 2.5 nm. The cutoff diameter is defined as the particle diameter at which 50% of particles are detected. The other two channels are equipped with more sensitive devices for detection of sub-2.5 nm particles. One channel is monitored by an Airmodus A10 Particle Size Magnifier in combination with an Airmodus A20 CPC and one by a TSI Nano-Enhancer 3777 combined with a 3772 butanol CPC. Both PSM and Nano-Enhancer use Diethylene Glycol as working fluid. A conservative estimation of the DMA-train's total time resolution lies in the order of 5 s. The DMA-train setup is commanded by a National Instruments Lab View (Version 2014 F) acquisition software, which sets parameters for all devices and stores the relevant data [7]. Based on the sizing data the GR calculation is then carried out using the appearance time method presented before.

4.2 Detectors and Devices

To provide a better understanding of the instrumentation, the subsequent section gives a more detailed insight into the functioning of the individual components of the DMA-train.

4.2.1 Particle Charger

To enable the classification of aerosols, the particles must be brought to a well defined charging state. To achieve this, a soft X-ray bipolar charger is employed in each layer of the DMA-train. Bipolar chargers, also referred to as neutralizers, are better suited for charging than unipolar chargers, since they produce significantly smaller amounts of multiple charges than their unipolar counterparts [32].

The 3088 Advanced Aerosol Neutralizer generates high concentrations of both positively and negatively charged ions (bipolar) using a soft X-ray source operating at low energy levels of less than 9.5 keV. These soft X-rays ionize air molecules resulting in nearly equal quantities of positive and negative charges.

Via the inlet port the aerosol is introduced into the neutralizer. Due to the process of diffusion, particles and air ions interact and exchange charges. Excess charges get neutralized, leading the aerosol to achieve a steady-state charge distribution [33].

4.2.2 Differential Mobility Analyzer

The Differential Mobility Analyzer was originally introduced to produce monodisperse submicron particles in order to calibrate other instruments [34].

Basically a DMA is designed as a capacitor to filter charged particles. The principle of that classification is based on the particles electric mobility Z:

$$Z = \frac{v_{\mathsf{E}}}{E} \tag{4.1}$$

v_{E} denotes the velocity a particle will reach in an electric field E [35].

According to [36] the electrical mobility for spherical particles with diameter d_{p} is given by:

$$Z = \frac{ieC_{\mathsf{c}}(d_{\mathsf{p}})}{3\pi\eta d_{\mathsf{p}}} \tag{4.2}$$

where i stands for the number of charges, e is the magnitude of the elementary unit of charge, C_{c} denotes the slip correction factor and η is the gas viscosity.

The slip correction factor, which is dependent by the particle diameter d_{p}, can be written as:

$$C_{\mathsf{c}} = 1 + \frac{2\lambda}{d_{\mathsf{p}}}\left(1.142 + 0.558\exp\left\{-\frac{0.999 d_{\mathsf{p}}}{2\lambda}\right\}\right) \tag{4.3}$$

where λ is the mean free path. C_{c} considers the non-continuum effects when the particle size becomes comparable or smaller than λ.

In the DMA-train setup, the cylindrically shaped Vienna type DMA is utilized, depicted as a schematic of a cross-section in Figure 7. The performance of such a DMA is characterized by two groups of parameters: its geometry (R_1, R_2, L) and its operating conditions (Q_{sh}, Q_{ex}, Q_a, Q_s).

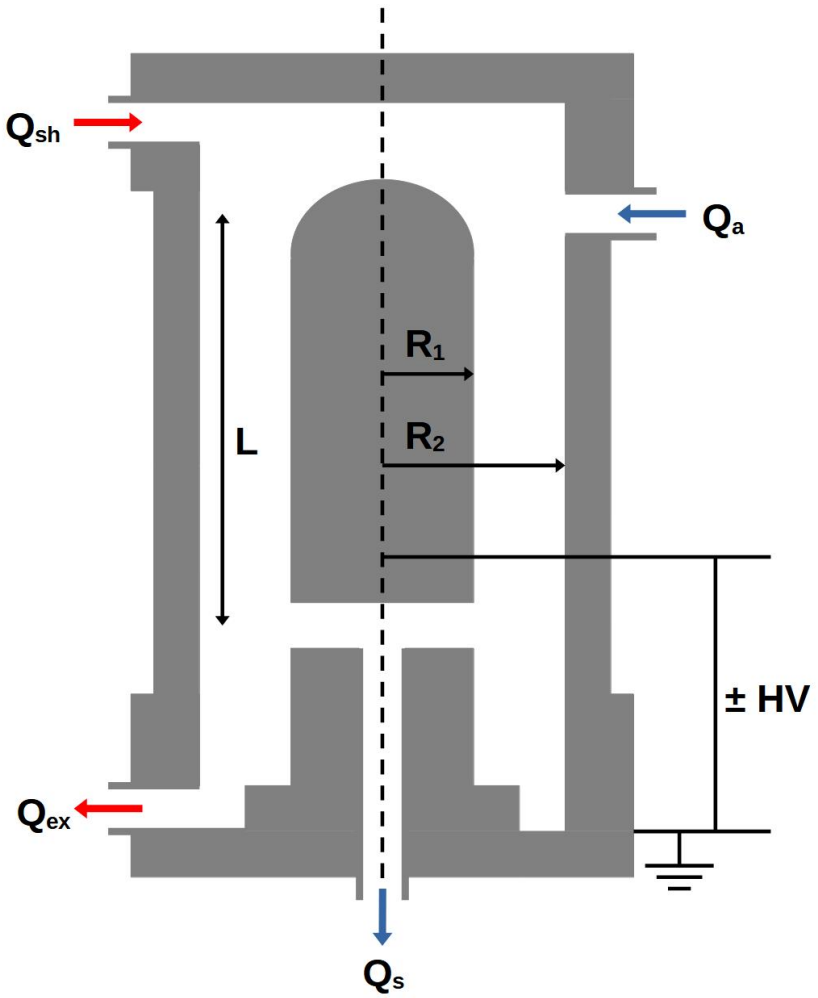

Figure 7: Schematic of a Vienna type DMA, based on [37]. R_1 and R_2 denote the radii of the inner and outer electrodes, L the effective axial distance between aerosol sample inlet and outlet. Q_{sh} represents the sheath air flow rate, Q_{ex} the excess air flow rate, Q_a the aerosol flow rate and Q_s the sample air flow rate. HV designates the applied high voltage necessary for particle selection.

The purified sheath air Q_{sh} enters the DMA tangentially on its top. After the inlet, a nylon screen is attached in order to achieve an effective laminarization of the sheath flow, what is crucial to operate the DMA correctly. The aerosol flow Q_a is introduced through an inlet port located in the outer electrode. Within the space between the two electrodes aerosol flow and sheath air flow are merged together very smoothly due to the curved shape of the inner space. A high voltage (up to ± 10kV) potential is applied to the inner electrode to provide the electrical field between the two electrodes. If geometry and operating conditions are fixed, the particles move into the direction of the electrical field corresponding to their electrical mobility Z. The classified particles leave the DMA-setup as sample air flow Q_s by a small outlet in the inner electrode. The residual air flow exits the DMA as excess air flow Q_{ex} at the bottom of the device [37][38].

Corresponding to [37] the electrical mobility Z of aerosol particles separated by the DMA is defined by the following relation:

$$Z = \frac{1}{V} \cdot \frac{\ln\left(R_2/R_1\right)}{2\pi L} \cdot \frac{\left(Q_{sh} + Q_{ex}\right)}{2} \tag{4.4}$$

where V denotes the voltage applied to the DMA.

4.2.3 Condensation Particle Counter

The Condensation Particle Counter (CPC) is commonly utilized to detect ultrafine particles within a diameter range of $\sim$ 5 nm to 1 μm [11].

CPCs use a supersaturated environment to grow aerosol particles in size until they become optically detectable. For this purpose the aerosol stream gets saturated by water or alcohol vapor. Then the instrument cools the aerosol down. Depending on the instrument, either adiabatic expansion or non-isothermal diffusion - achieved by flow through a cold tube - are used to reach the level of supersaturation needed for nucleation and growth. Each aerosol particle grows to a droplet, hence the number concentration keeps unchanged during that process. The number concentration of droplets is finally determined by

single particle optical counters or light-transmission measurements [1].

The CPC models installed in the DMA train - TSI 3776, TSI 3772, and Airmodus A20 - all operate using butanol as working fluid. Figure 8 illustrates the schematic framework of a TSI model 3776 CPC, which is optimized for particle detection in the sub-3 nm range [39].

An integrated high-vacuum pump enables a constant inlet flow of either 1.5 l/min (high flow mode) or 0.3 l/min (low flow mode), with the DMA-train using the first option in order to improve response time and minimize particle losses. After the inlet the flow is parted into 0.3 l/min sample flow through the sensor as well as 1.2 l/min bypass flow. The sensor flow is then split again into a 0.25 l/min sheath flow and a 0.05 l/min aerosol flow. A HEPA filter is used to clean the sheath flow just before it gets drawn into the saturator where a liquid-soaked, heated wick saturates the sample with butanol vapor. Right in front of the condenser sheath flow and aerosol flow are recombined. The cooled condenser allows the butanol vapor to condense onto the particles, causing them to grow in size. Now the droplets can be easily detected by the heated optical sensor. The cutoff diameter of this model is 2.5 nm [40].

In contrast to the model TSI 3776, TSI 3772 and Airmodus A20 are laminar-type CPCs. That means that instead of splitting the flow, the entire sample stream is heated and saturated with butanol vapor. As the next step, the saturated sample flow is directed to a multi-tube condenser - 8 tubes in the TSI 3772 model, 6 in the Airmodus A20 model - where it is cooled down and growth occurs before optical detection takes place. The nominal cut-off diameters for these instruments are 10 nm and 7 nm respectively. The inlet flow rate is 1 lpm. The factory temperature settings are 39°C for the saturator, 22°C for the condenser, and 40°C for the optics in the 3772 model; and 39°C for the saturator, 15°C for the condenser, and 40°C for the optics in the A20 model [39].

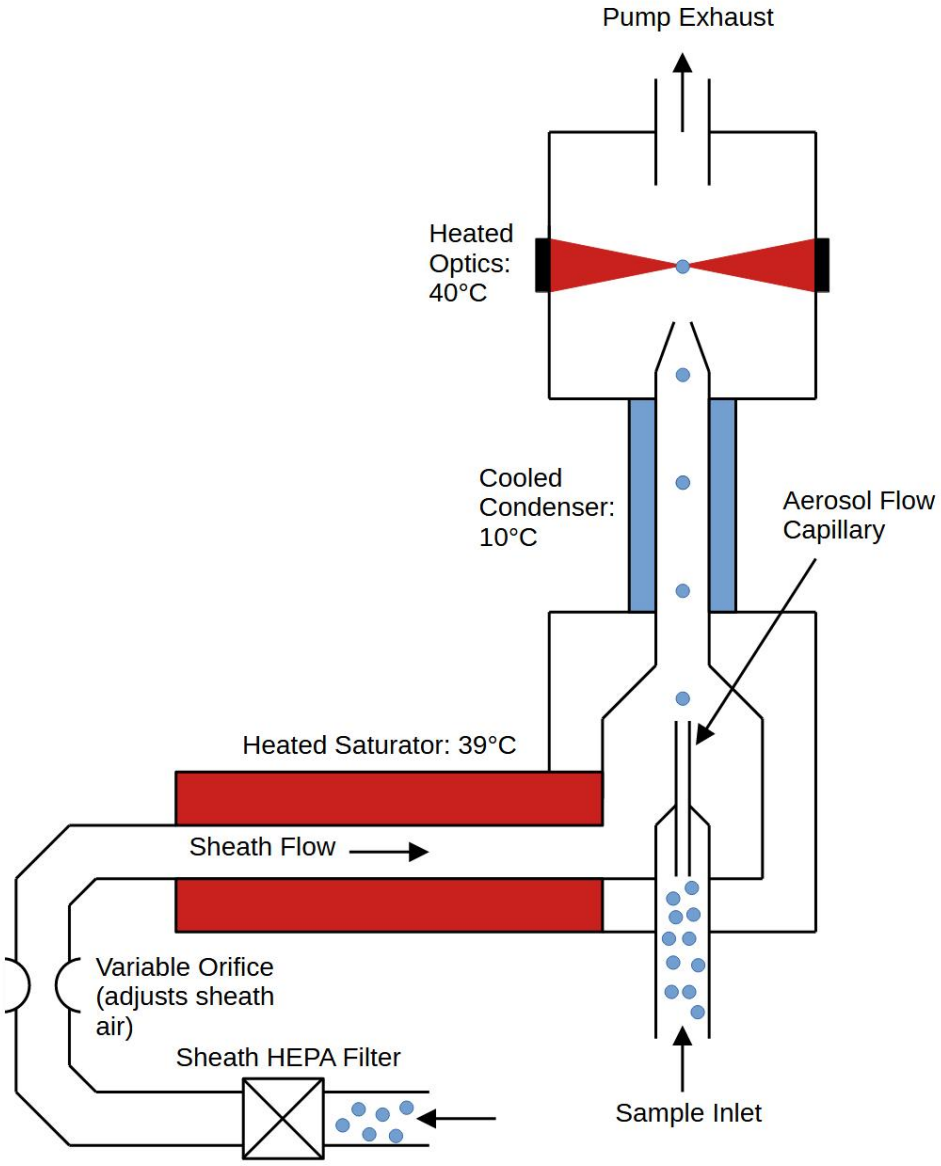

Figure 8: Schematic of the TSI model 3776 Ultrafine Condensation Particle Counter. Based on [40].

4.2.4 Particle Size Magnifier

A Particle Size Magnifier (PSM) is an aerosol pre-conditioner, that enables to grow aerosol particles from sizes as small as 1 nm up to 90 nm. The resulting particles are then large enough to be detected by a CPC. The DMA-train setup uses a combination of Airmodus A10 PSM and Airmodus A20 CPC for the smallest size channel (nano Condensation Nucleus Counter system MODEL A11 nCNC).

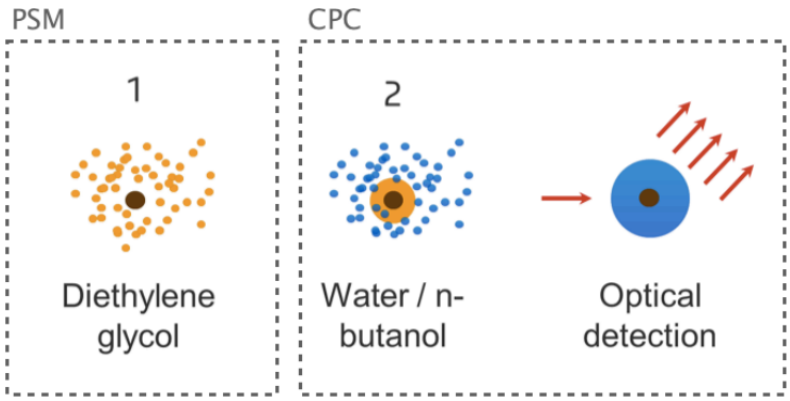

Figure 9: Schematic of the two-stage PSM-CPC combination [41].

The main difference is the working fluid used to grow the aerosol particles. Diethylene Glycol (DEG) condenses more easily onto nano particles than butanol or water, thus the PSM can activate much smaller particles than CPCs. However, growth terminates at ~ 90 nm due to the low saturation vapour pressure of DEG. There is no longer enough DEG vapour to allow the particles to continue growing. DEG is also less toxic and corrosive than butanol. Furthermore the PSM has no optical counting system.

Purified air is drawn into a saturator where it gets heated and exposed to vaporized DEG. Inside a cooled mixing region, the saturator flow is turbulently merged with the aerosol sample flow. Instead of using critical orifices, the PSM flow rates are controlled by Mass Flow Controllers (MFC). Following the mixing region the recombined flow passes a cooled growth tube, where the particles continue to grow. Finally a part of the flow that leaves the PSM is directed to the CPC, while the remaining part is disposed as excess flow [41].

In Figure 10 a schematic of the combined Airmodus counter system is depicted.

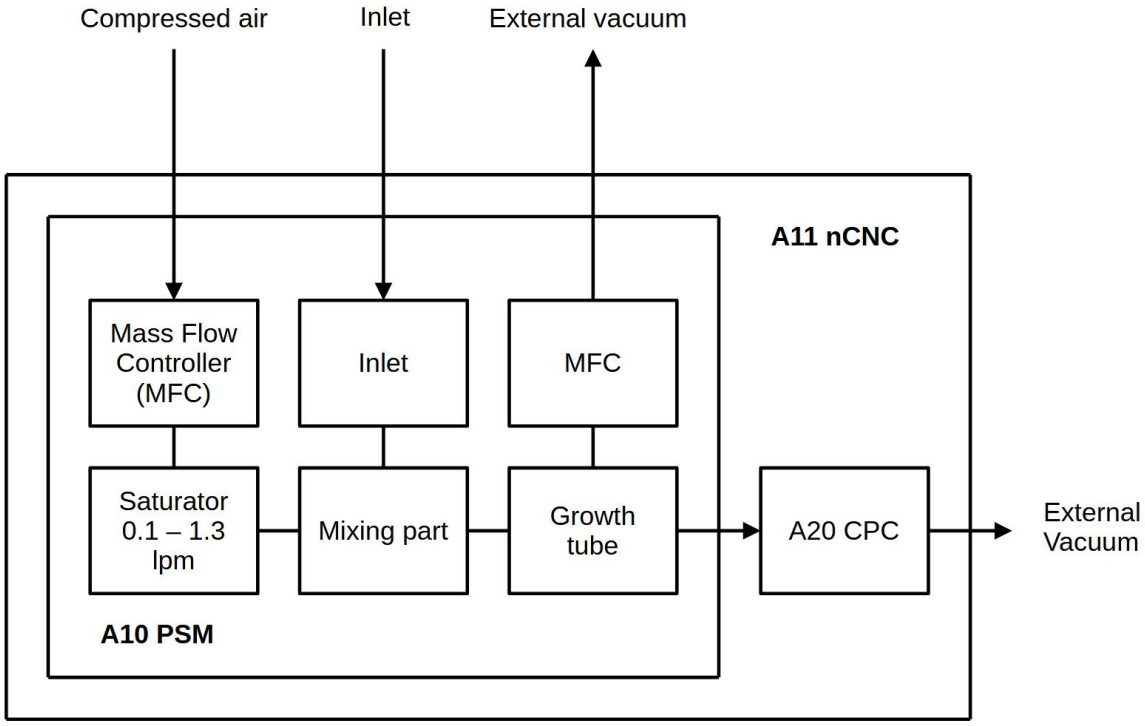

Figure 10: Schematic of the Airmodus A10 PSM, including saturator, mixing region, growth tube and CPC. Figure based on [41].

4.2.5 Nano-Enhancer

A Nano-Enhancer is a device capable of counting particles down to a geometric diameter of 1 nm when used in combination with a CPC. The DMA-train operates with a TSI 3777 Nano-Enhancer combined with a TSI Model 3772 CPC. The working principle is roughly the same as that of the PSM and will be explained in the following lines.

Through an inlet port the aerosol sample is drawn into the Nano-Enhancer and mixed with purified, dry sheath air. The flow moves through a heated saturator where DEG vaporizes and dissolves within the sheath air. In a cooled condenser the DEG vapor achieves supersaturation and gets ready to con-

dense onto the aerosol particles serving as condensation nuclei. When the newly formed droplets reach a threshold diameter, they grow large enough to be detected by the CPC [42].

Figure 11 shows a schematic of the operation principle of the used Nano-Enhancer.

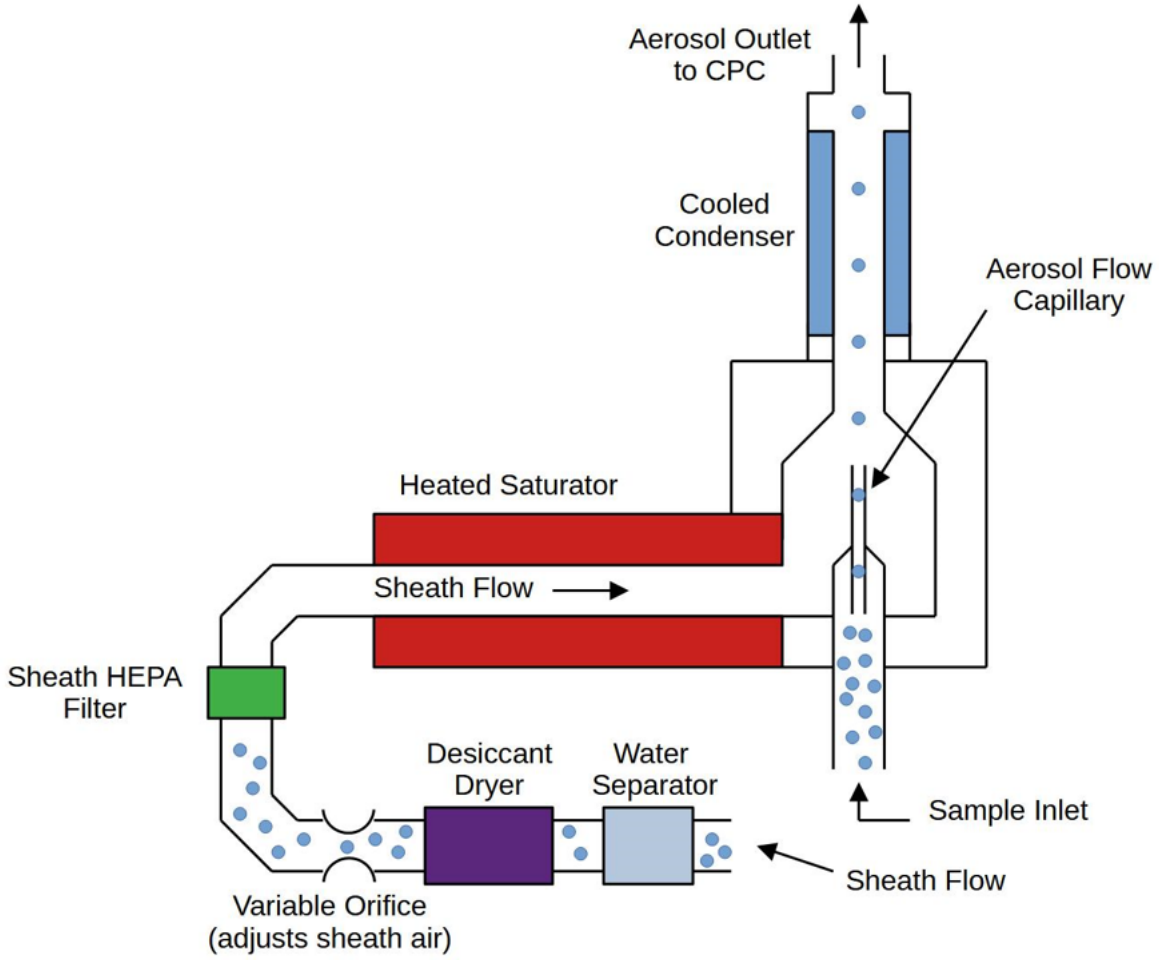

Figure 11: Schematic of the TSI 3777 Nano-Enhancer. Figure based on [42].

4.3 Neutral cluster and Air Ion Spectrometer

No direct measurements with the Neutral cluster and Air Ion Spectrometer (NAIS) were performed for this master's thesis. However, since comparative data were used, the mode of operation of this device is also important for a full understanding of the matter.

The NAIS is an instrument to measure mobility distributions of charged particles of both polarities in an electrical mobility range from 3.2 to 0.0013 $cm^2V^{-1}s^{-1}$ as well as size distributions of total particles in a size range from 2.0 to 42 nm [43]. It uses the principle of electrical aerosol spectrometry.

According to [44] electrical aerosol instruments evaluate total concentrations of particles using a known probability distribution of electric charge on a particle after the aerosol has undergone charging under well-defined conditions. The particles are then measured based on the electric charge they carry. The huge advantage of this method is the size independent detection of particles by measuring their electric charge. Therefore, the typical 3 nm limitation of CPCs can be avoided.

The NAIS is made up of two parallel operating electrical mobility analyzer columns, which are only distinguished by the polarity of the measured ions. After the classification the aerosol is detected by an array of 21 electrometers per column [44]. The mobility analyzer is equipped with a software-commanded precondition unit. This system sorts out certain ions of the aerosol depending on the measuring method [43].

There are four different main measurement methods:

1. Ions mode: used to detect naturally charged particles. No preconditioning, the sample is not modified.
2. Particles mode: all particles are measured, even the initially uncharged ones. Main charger and post-filter are activated. The main charger charges all particles, which can then be detected. The post filter is provided to remove the excess ions from the charger.
3. Alternating charging mode: similar to particles mode but with better instrument performance. The discharger is switched on additionally.
4. Offset mode: in this mode no particles enter the analyzer to measure zero signal and noise levels of the instrument [43].

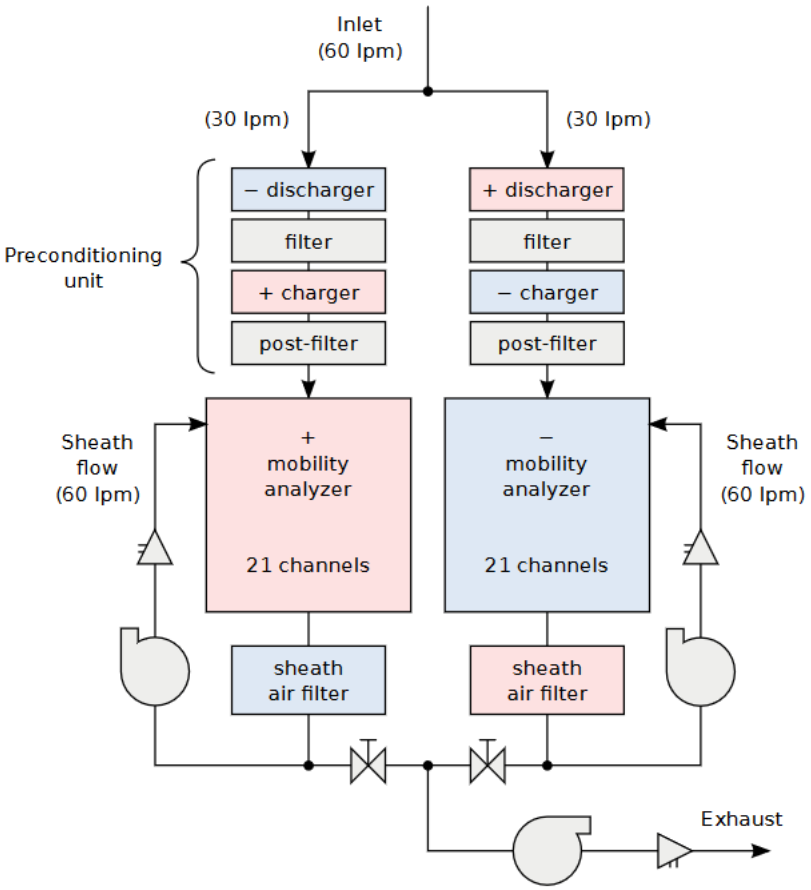

Figure 12: Schematic of the NAIS [44].

Due to a quite high sample flow rate, the NAIS achieves a high time resolution of 1 s or better and keeps ion cluster losses low. The instrument works very reliably at medium and high particle concentrations, but a certain amount of background noise occurs at lower concentrations. A further issue of the NAIS is that charger ions have the same mobility as sub-2 nm particles. This results in a lower detection limit for neutral particles [44].

4.4 Nitrate Chemical Ionization Atmospheric Pressure interface Time-Of-Flight mass spectrometer

The nitrate CI-APi-TOF is a mass spectrometer which is used to determine sulfuric acid, HOM and VOC concentrations during CLOUD measurement campaigns. At CERN the instrument is provided and maintained by the Goethe University of Frankfurt. According to [45] the CI-APi-TOF consists of three main elements, which are:

1. a custom-made inlet for chemical ionization at ambient air pressure (CI),
2. an atmospheric pressure interface (APi) and
3. a time-of-flight mass spectrometer (TOF).

However, the CLOUD CI-APi-TOF utilizes a LTOF (long time of flight mass spectrometer), that offers a wide mass range up to 2000 Th and a very high mass resolving power (up to ca. 12000 Th/Th) [46]. The sample is sucked in through a stainless steel tube at a flow rate around 10 lpm. By exposing clean air mixed with nitric acid (20 lpm) to alpha radiation from a 10 MBq ^{241}Am source nitrate ions are formed [45]. The ion source uses a corona discharge needle to produce the charged nitrate particles [46]. The sheath flow is then fed into an ion reaction tube that is positioned concentrically to the sample flow. An electric field guides the nitrate ions into the sample flow with an interaction time of approximately 200 ms between ions and sample gas. In the CI system, ionization takes place at ambient pressure through proton

transfer between nitrate ions or their clusters with nitric acid and sulfuric acid, resulting in the formation of bisulfate ion-nitric acid clusters and neutral nitric acid [45]. In the APi part the air sample flows through a critical orifice at a rate of 0.8 lpm. Following this, the ions are led by two quadrupoles and an ion lens into the mass analyzer. In this interface, the pressure gradually drops from atmospheric levels to 10^{-6} hPa inside the mass spectrometer [47], where the sample is sorted based on its m/z ratio [45]. A schematic of the University of Frankfurt CI-APi-TOF is illustrated in Figure 13.

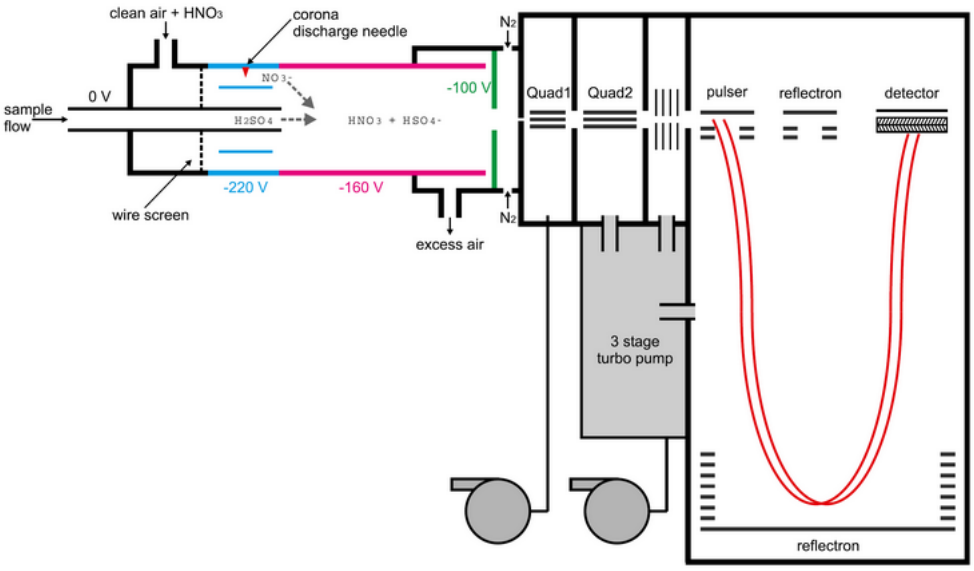

Figure 13: Schematic of the CI-APi-TOF used at CLOUD campaigns [46].

4.5 PTR3 - Proton Transfer Reaction-Time-Of-Flight Mass Spectrometer

The PTR3 is a newly developed form of Chemical Ionization Time-Of-Flight mass spectrometry that can be used to detect low traces of VOCs, HOMS and their oxidation products. The basic concept of the PTR3 is to separate the reaction chemistry from the axial transport of the ions in order to improve the overall sensitivity of the tool [48]. This is realised by using a tripole in the reaction chamber operated with rf (radio frequency) voltages to create a rotating electric field only in radial direction [49]. Conventional PTR mass spectrometers, however, use axial DC drift fields to ionize samples in a re-

action area. In PTR3 the axial movement of the ions is only dependent of the sample gas flow leading to an extended reaction time and therefore to enhanced sensitivities. A dual stage core sampling inlet allows samples to be injected without wall contact, ensuring that the transport into the PTR3 reaction chamber is carried out with minimal loss and surface interaction [48]. The ion source consists of a corona discharge as well as a source drift region to transfer primary ions to the tripole reaction chamber. Humidified nitrogen, which acts as ionization gas is added in immediate distance. The sample gas flow of the instrument is 10 lpm, the sheath flow 8 lpm. A pressure drop occurs in the drift region caused by the gas flows through the exit lens of the reaction chamber, decreasing from 80 to 4 mbar. This prepares the coupling of the PTR3 to a single LTOF mass spectrometer [49]. The instrument reaches resolving powers up to 10000 to 15000 Th/Th [48].

During the CLOUD campaign the PTR3 is operated and maintained by the University of Innsbruck, who also developed it. An illustration of a PTR3 is depicted in Figure 14. The α-pinene data used in this thesis were obtained with the PTR3.

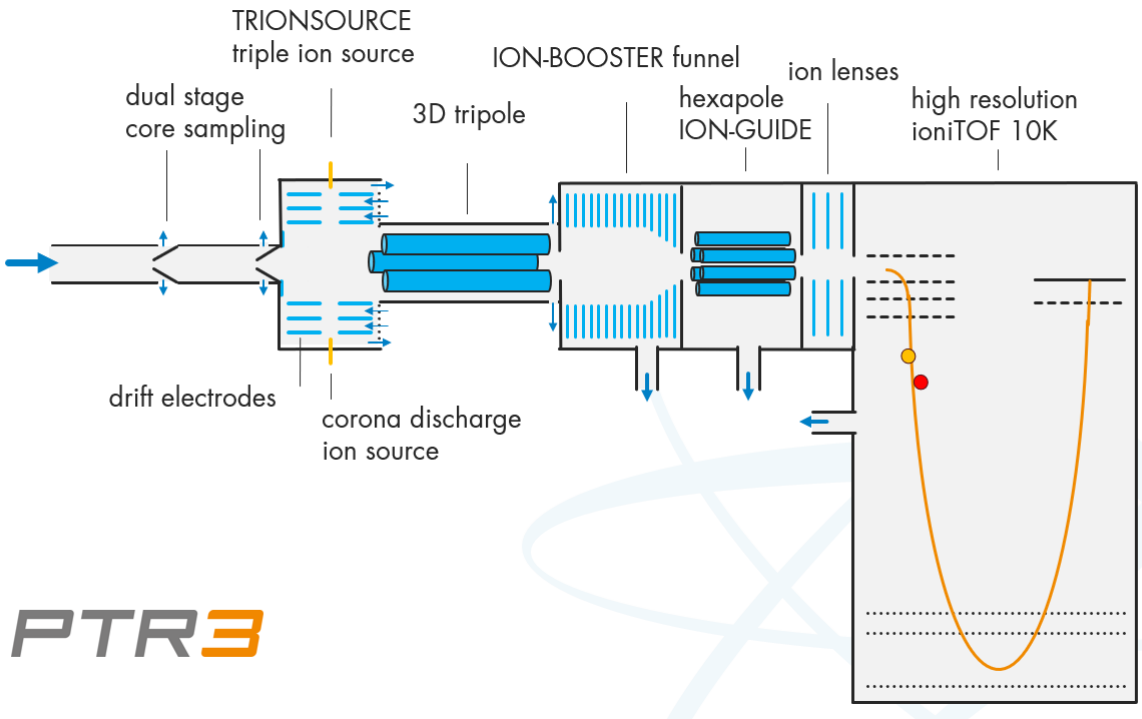

Figure 14: Schematic representation of a PTR3 version from IONICON [48].

4.6 Thermo Environmental Instruments Model 49C

The TEI49C is an UV photometric ozone analyzer to measure the ozone concentrations in the CLOUD chamber. The ozone in the chamber reacts with α-pinene and forms aerosol particles. The instrument works on the principle that ozone molecules absorb UV light at a wavelength of 254 nm. The extent of the UV light absorption is directly correlated with the ozone concentration. This relation is defined by the Beer-Lambert law:

$$\frac{I}{I_0} = e^{-KL^*C} \tag{4.5}$$

where K is the molecular absorption coefficient, 308 cm^{-1} at 0°C and standard atmosphere pressure, L^* is the length of the cell with 38 cm, C is the ozone concentration in ppm, I is the UV intensity in the sample gas and I_0 the intensity in the reference gas.

After the sample is injected into the TEI49C through the inlet, it is divided into two parallel gas streams. One stream flows through the ozone scrubber to absorb a specific amount of ozone and thus turns into the reference gas. Then both streams reach a separate solenoid valve. Every 10 seconds, the solenoid valves switch the reference and sample gas streams between cells A and B. For instance, when cell A holds the reference gas, cell B contains the sample gas, and vice versa. Detectors A and B measure the corresponding UV intensities. Model TEI49C calculates the ozone concentrations for each cell and then provides the averaged ozone concentration [50]. An corresponding illustration of the operation principle is shown in Figure 15.

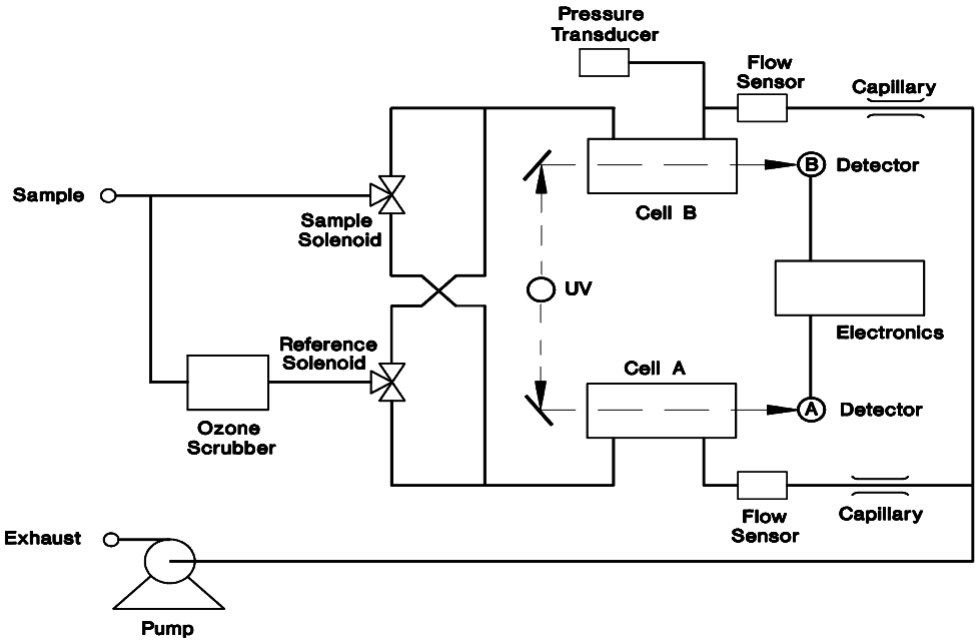

Figure 15: Schematic of the Model TEI49C ozone analyzer [50].

5 | Growth Rate Evaluation and Results

This chapter describes how to obtain the growth rates of the CLOUD16T baseline measurements as well as ways to compare the measurement data with two different campaigns. The data sets to be used for comparison are taken from CLOUD12 and CLOUD15, whereby the CLOUD12 data has already been evaluated and published in [7]. CLOUD12 took place in the beginning of 2018, CLOUD15 in fall 2022.

5.1 Calculation of the Growth Rates

The following section illustrates how the growth rates of the baseline runs 2508.06 and 2509.01 were calculated. The identification numbers are a combination of the run number and the corresponding stage number. For small changes in the CLOUD chamber (e.g. fans on/off, change of gas injection rate,...), a new stage (number after the dot) is usually started. For larger changes (e.g. beam on/off, injection of another gas,...), a new run (number before the dot) is initiated. Due to low aerosol particle concentrations, the third baseline run (neutral) could not be analysed. To obtain the GRs, two different size intervals were defined for the DMA-train: one from 1.8 nm to 3.2 nm and another one from 3.2 nm to 8.0 nm. Although the selection of these intervals is arbitrary, it has been demonstrated to effectively highlight differences between early and later growth stages [6].

The temperature during CLOUD16T remained constant at 5°C. Figure 16 shows the gas concentration development over time of the substances covered

in the sections below. The red dotted lines in Figure 16 mark the two baseline runs. Also visible are the times at which α-pinene (only small peaks) and ozone were fed into the chamber to perform ozonolysis experiments. When the α-pinene enters the chamber, it can be observed how the concentrations of HOM and VOC slowly begin to emerge. Both HOM and VOC are classified as explained in chapter 3.3. At certain times, the ozone curve is in the negative range. At these times, the TEI49C either had problems with pressure or flow or, more likely, the ozone data has not yet been calibrated to the zero point.

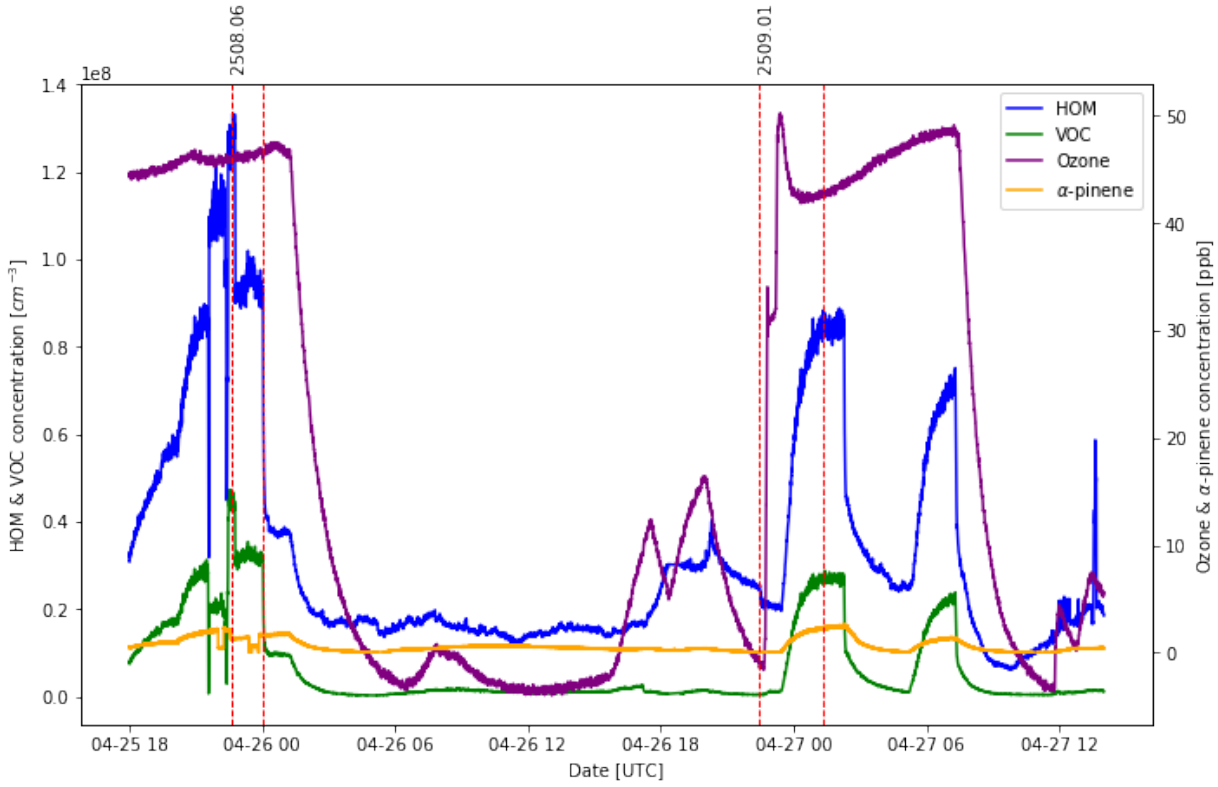

Figure 16: Gas concentration development over time of HOMs, VOCs (in cm^{-3}), Ozone and α-pinene (in ppb) during the CLOUD16T campaign.

For the evaluations the concentrations of the substances have to be more or less constant over the period in which the particle growth takes place. To check this and since the α-pinene peaks are only very small, runs 2508.06 and 2509.01 are displayed again magnified with the time spots of aerosol particle growth outlined (red dotted lines in Figures 17 and 18). Figure 17 shows the time of particle growth during run 2508.06. During the particle growth all the gases look sufficiently constant. At the beginning of the plot, the injection of α-pinene can be detected. A small increase of HOMs and VOCs is visible as

well. The increase is that low because a neutral run took place before this run, in which particle growth had already occurred. The jumps that appear before the measured particle growth are remarkable and actually do not behave as expected. However, these can be explained quite simply. According to the logbook the settings of PTR3 and CI Api-TOF were changed just before the initial particle growth. Regarding further analyses, these definitely must be corrected.

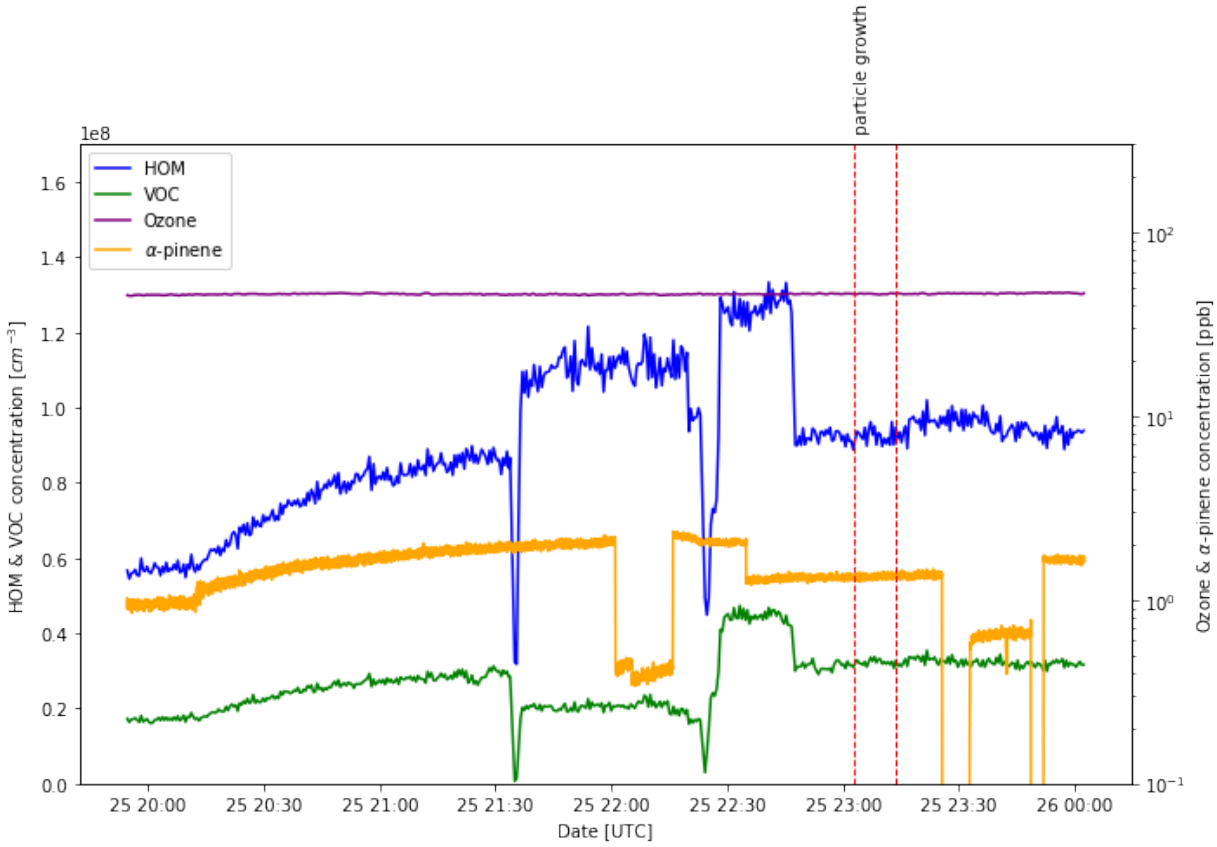

Figure 17: Gas oncentrations for run 2508.06.

In contrast to run 2508.06, there are no jumps in plot 18 and the progression of the experiment is clearly visible. After the ozone has reached a constant concentration, AP is introduced and consequently VOCs and HOMs are produced. HOMs and VOCs from run 2509.01 are not completely constant and the GR measurement took place during ozonolysis. However, the differences are marginal and here as well the mean values were used for the further data analysis.

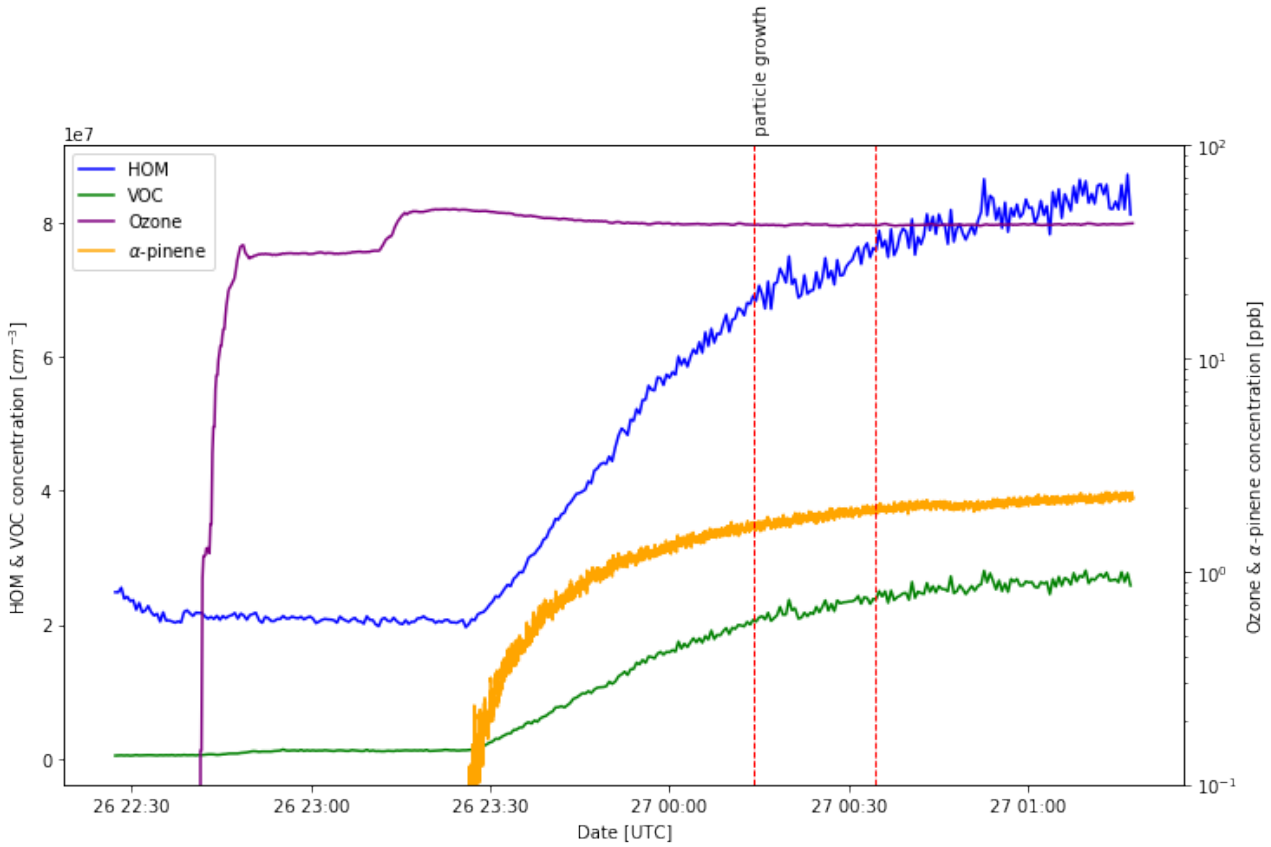

Figure 18: Gas concentrations for run 2509.01.

5.1.1 Run 2508.06

Run 2508.06 is a GCR run, that means fans and PS are switched off and the contents of the CLOUD chamber only interact with galactic cosmic rays. In Figure 19 the fit of the 2.2 nm size channel of run 2508.06 is depicted as a representative of all seven channels. As mentioned previously, a sigmoid function is applied to obtain the corresponding appearance times.

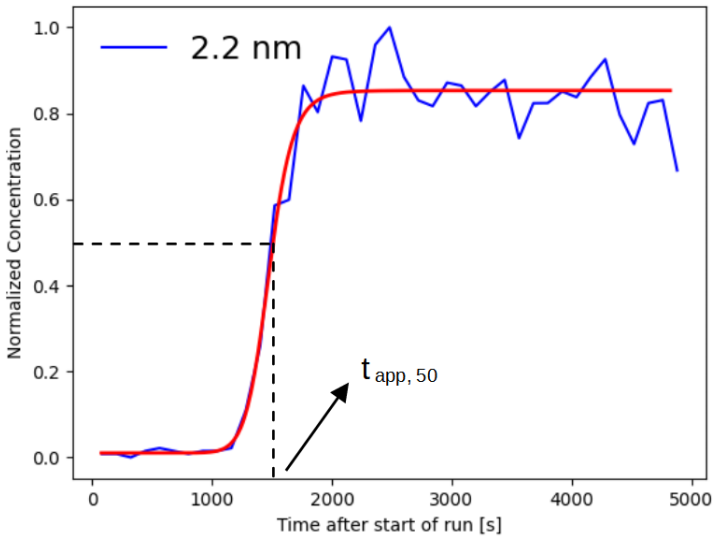

Figure 19: Sigmoid function fit to the measured aerosol particle concentration within the 2.2 nm channel. Here is also shown how to obtain the corresponding appearance time t_{app50}.

The appearance times of different particle sizes are then plotted and used to perform a linear regression. The slopes in both size intervals, shown in Figure 20, are then equivalent to the growth rates during the experiment. The given error results from the statistical uncertainty of the appearance times.

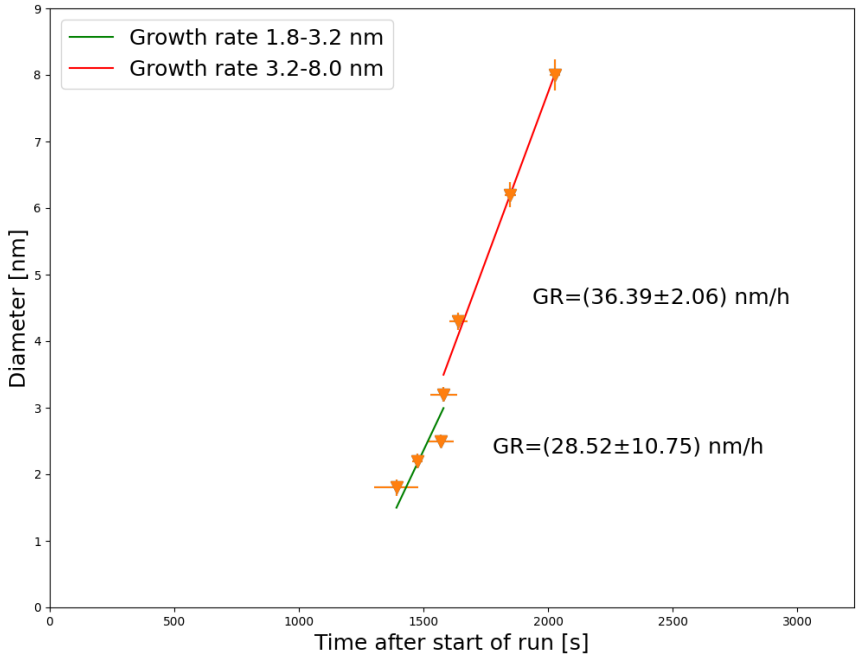

Figure 20: Orthogonal distance regression for the growth rate determination in two intervals.

As expected, a size difference in the GRs can be detected. However, in the interval [1.8-3.2] nm, it is evident that the GR has a relatively large statistical error. The appearance time of channel 2.5 nm seems to be clearly further away from the fit than the others. This can most likely be explained by the low number of counts at this size.

Figure 21 confirms the particle growth event in form of a banana-type contour plot. The red areas illustrate high concentrations of particles, the blue areas illustrate low concentrations. An increase in particle concentrations can be observed in each channel, along with some background noise in the first channel.

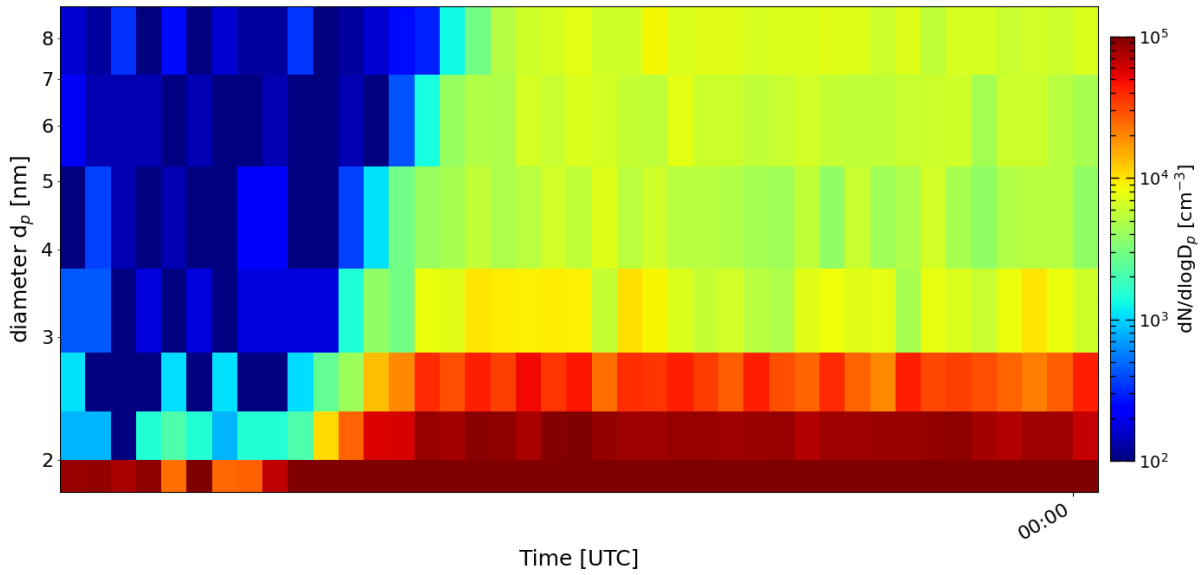

Figure 21: Contour plot run 2508.06.

5.1.2 Run 2509.01

Run 2509.01 is a beam run which means the PS beam was switched on during the measurement, leading to ionization of the aerosol particles. Run 2509.01 is analysed in the same way as run 2508.06 previously. Figure 22 shows the 1.8 nm channel with corresponding Sigmoid fit.

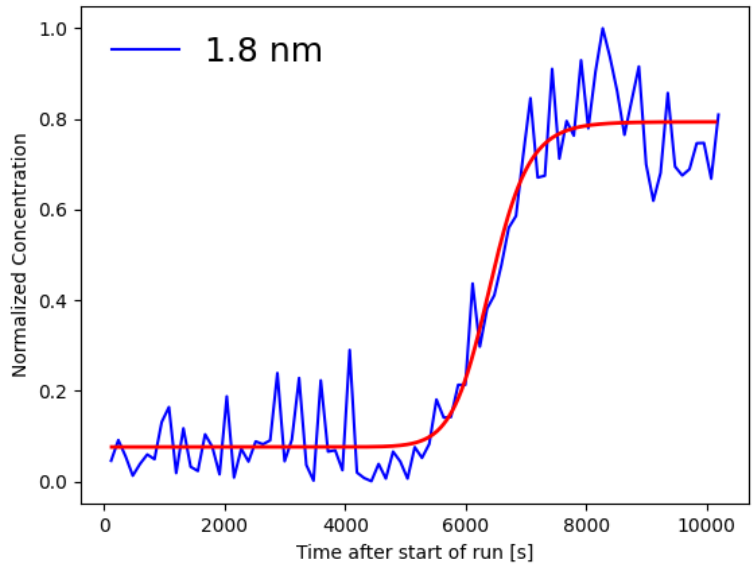

Figure 22: Sigmoid function fit to the measured aerosol particle concentration within the 1.8 nm channel.

Orthogonal distance regression and growth rates are depicted in Figure 23.

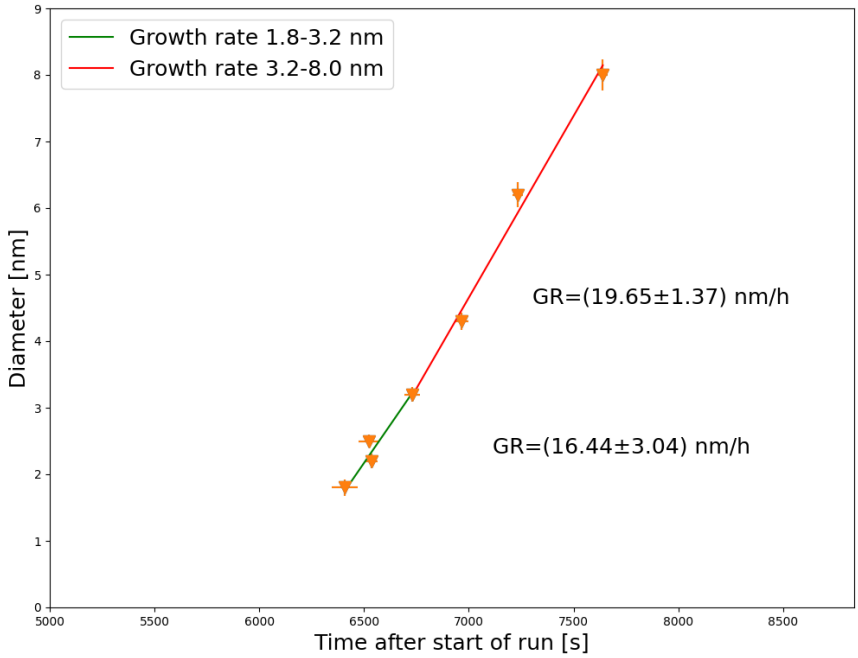

Figure 23: Orthogonal distance regression for the growth rate determination in two intervals.

Again, a difference in size can be observed in the two GRs. In contrast, there is less statistical error. It can be assumed that the increased number of ions, due to the activated PS results in a higher number of counts, which consequently reduces the statistical error.

Eventually, the contour plot of run 2509.01 is illustrated in Figure 24.

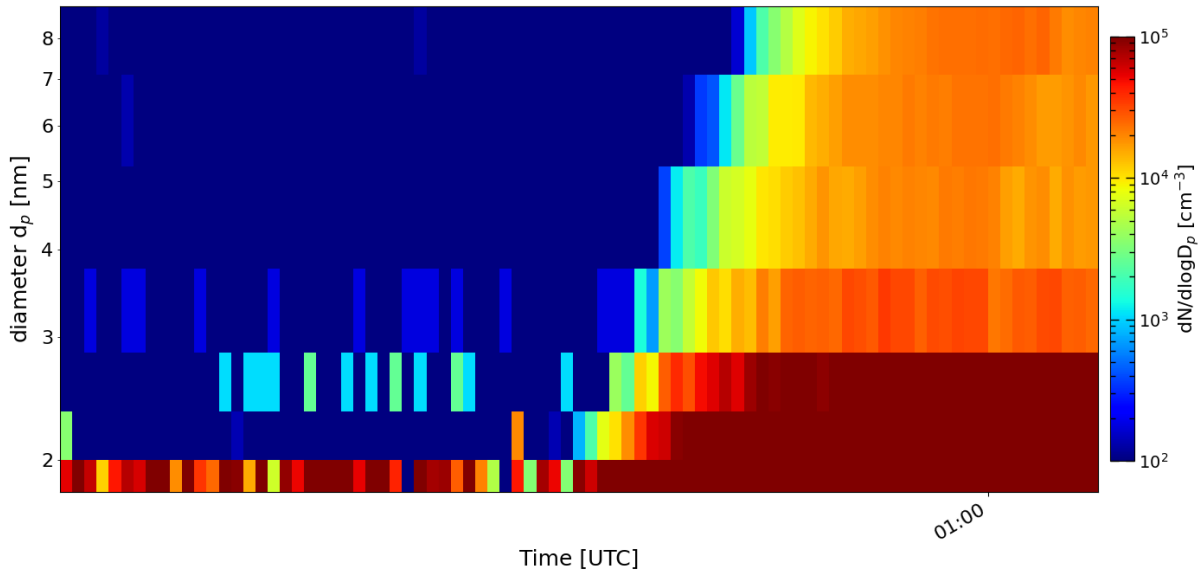

Figure 24: Contour plot run 2509.01.

A quick look at Figure 24 shows that background noise can always be present. Certain signals were detected by the DMA-train just before the particle growth event had started. Especially the smallest channel at the bottom of the Figure looks incompatible. Of course, it is also possible that the CLOUD chamber was not cleaned sufficiently and residuals from the previous run are responsible for the signals. However, it is more likely the PSM CPC combination has worked erratically and is responsible for the background. Concerning the evaluation, a constant background noise has no influence on the GR calculation. Since the evaluation program normalises each size channel to the corresponding maximum, the background can therefore be neglected.

For a better overview, the growth rates, along with their statistical uncertainties, are presented again in the following Table 2.

Interval	Run 2508.06	Run 2509.01
[1.8-3.2] nm	(28.52 ± 10.75) nmh^{-1}	(16.44 ± 3.04) nmh^{-1}
[3.2-8.0] nm	(36.39 ± 2.06) nmh^{-1}	(19.65 ± 1.37) nmh^{-1}

Table 2: Growth rates obtained with the DMA-train.

5.2 Comparison of DMA-train and NAIS

In this section, the obtained growth rates of two different instruments are compared. In Figure 25, the GRs in the interval [3.2-8.0] nm measured by DMA-train and NAIS respectively are plotted against each other. The calculation of the GRs is in both cases based on the appearance time method.

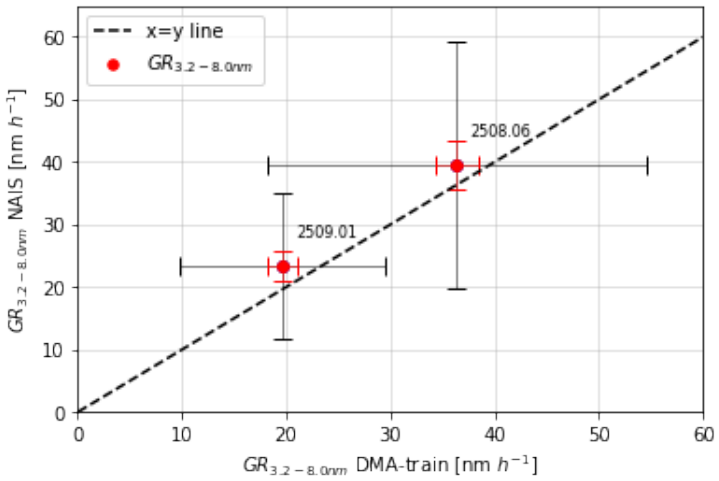

Figure 25: DMA-train GRs plotted versus NAIS GRs.

Since the size range of the NAIS extends from 2-42 nm and the required concentration to detect particles of 2-3 nm is very high in order to obtain accurate data [43], it is more practical to compare GRs in the interval [3.2-8.0] nm. The red error bars correspond to the statistical uncertainty, the black error bars give the 50 % systematic uncertainty of the appearance time method [6]. Considering the small deviation of the data points from the x=y line, a good agreement of the measured GRs can be observed, as it can be verified in publication [7]. Table 3 highlights the obtained growth rates as well as their difference in % again.

Run	DMA-train	NAIS	Difference in %
2508.06	(36.39 ± 2.06) nmh^{-1}	(39.43 ± 3.94) nmh^{-1}	7.71 %
2509.01	(19.65 ± 1.37) nmh^{-1}	(23.30 ± 2.33) nmh^{-1}	15.67 %

Table 3: Growth rates in the interval [3.2-8.0] nm measured with DMA-train and NAIS respectively.

5.3 Growth Rates versus Several Gas-Phase Variables

The below sections analyse the comparison of growth rates with different gas-phase variables. The measurement campaigns are comparable since the experiments were conducted under nearly identical conditions. α-pinene ozonolysis experiments were performed at a constant temperature of 5°C. In general, the comparisons serve the purpose of verifying the instruments involved. Furthermore, it is advantageous to measure certain variables several times in order to draw statistical conclusions. The data points of the CLOUD12 and the CLOUD15 campaign are in each case taken from GCR or beam stages. Beam and CGR runs can be compared since the GRs are relatively independent of the charge states of the molecules, which is outlined more detailed in [51].

5.3.1 α-pinene Ozonolysis Reaction Rate Comparison

In Figures 26 and 27 the correlation of the growth rates with the estimated reaction rate of the α-pinene ozonolysis is shown. Higher reaction rates lead to higher product concentrations and thus lead to higher growth rates. As described in publication [7], the GRs follow an exponential relation:

$$GR = m(T, d_{\mathrm{p}}) \cdot (k(T) \cdot [ap] \cdot [O_3])^{\mathrm{q}} \tag{5.1}$$

[ap] and $[O_3]$ are the α-pinene and O_3 concentrations in cm^{-3}. The coefficients k(T) and $m(T, d_{\mathrm{p}})$ depend on temperature respectively on temperature and particle diameter. k(T) denotes the corresponding rate constant and $m(T, d_{\mathrm{p}})$ as well as the reaction order q are empirical parameters resulting from the least square regression. The illustrations show two dotted lines representing the exponential relation, one (blue) with q ($\mathrm{q}_{\mathrm{CLOUD12}}$) taken from [6] and one (black) with a q ($\mathrm{q}_{\mathrm{all}}$) obtained by least-square regression of all data points. $m(T, d_{\mathrm{p}})$ is also taken from [6], k(T) calculated according to [52]. The applied values are summarised in Table 4.

	m(5°C)	$q_{CLOUD12}$	q_{all}	k(5°C)
[1.8-3.2] nm	$2.09 \cdot 10^{-7}$	1.21	1.24	$7.14 \cdot 10^{-17}$
[3.2-8.0] nm	$3.12 \cdot 10^{-7}$	1.21	1.25	$7.14 \cdot 10^{-17}$

Table 4: Parameters for the exponential relation $GR = m(T, d_p) \cdot (k(T) \cdot [ap] \cdot [O_3])^q$.

In the below plots the blue dots correspond to CLOUD12, the green ones to CLOUD15 and the red points to CLOUD16T.

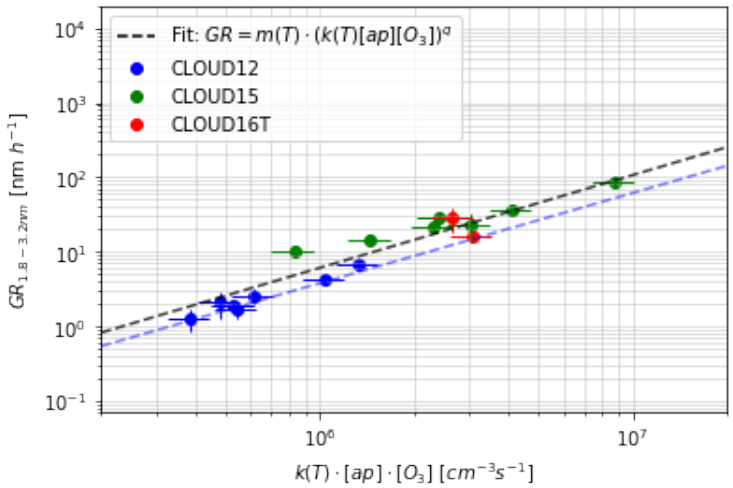

Figure 26: Correlation with the estimated reaction rate of the α-pinene ozonolysis for the interval [1.8-3.2] nm during the growth rate measurement. The blue dotted line corresponds to the q from [6], the black dotted line takes all the measurement points into account.

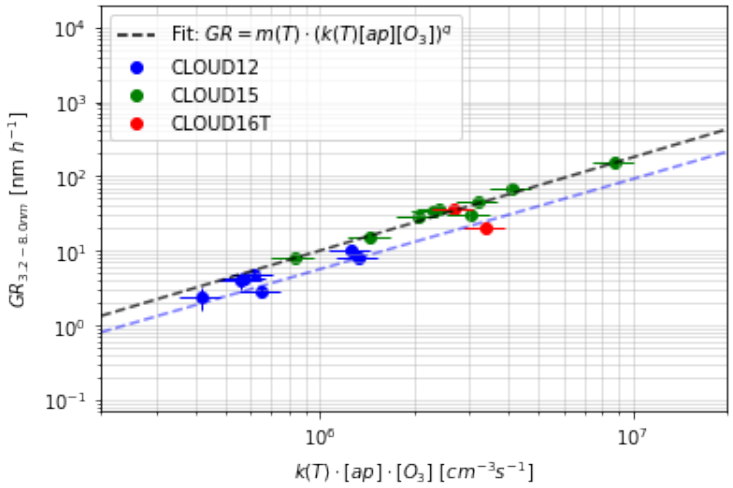

Figure 27: Correlation with the estimated reaction rate of the α-pinene ozonolysis for the interval [3.2-8.0] nm during the growth rate measurement. The blue dotted line corresponds to the q from [6], the black dotted line takes all the measurement points into account.

The x-axis error is calculated from the instrument errors by Gaussian error propagation. The uncertainty of the α-pinene measurement of 15 % was taken from [53]. That of the O_3 measurement - 1 ppb - from the operating instructions of the ozone monitor [50]. Both figures follow the same pattern presented in publication [6]. q_{all} differs only minimally from $q_{CLOUD12}$. The data points of CLOUD16T show a reverse trend at first glance. However, experimental data always have a certain amount of scatter that must be taken into account.

5.3.2 HOM Comparison

Figures 28 and 29 show the total HOM concentrations observed in the nitrate CI-APi-TOF versus the measured growth rates. Figure 28 shows interval [1.8-3.2] nm, Figure 29 interval [3.2-8.0] nm.

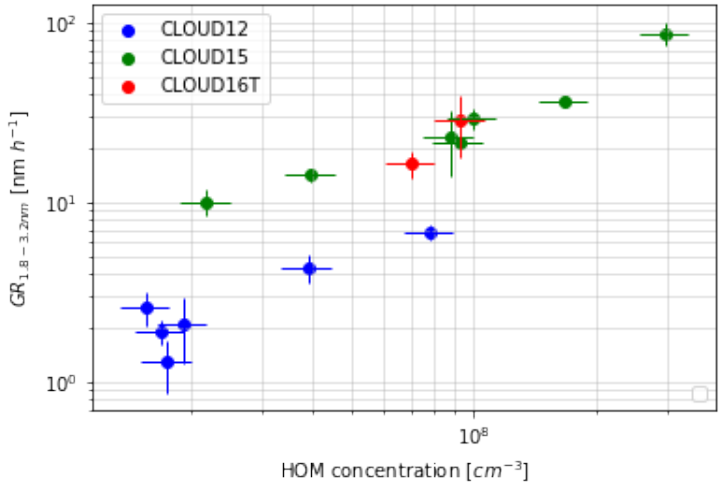

Figure 28: GRs vs. HOM concentration in the interval [1.8-3.2] nm.

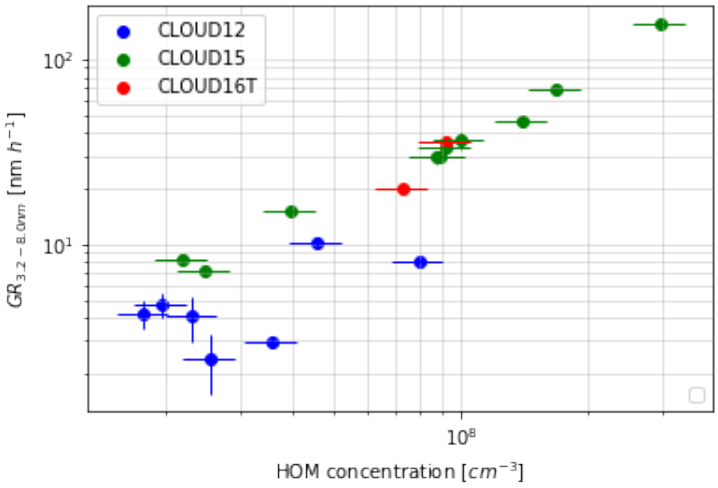

Figure 29: GRs vs. HOM concentration in the interval [3.2-8.0] nm.

Especially in Figure 28, it can be clearly observed that the GRs increase as expected with increasing HOM concentration. The error of the HOM concentrations results from the instrument error of the CI-APi-TOF, which is 14% according to [54]. It is notable that the measurement points of the CLOUD12 campaign are significantly below the other two measurement series. Figure 29 seems to depict the same pattern, except the measurement points from CLOUD12 which show a less clear trend. However, the baseline measurements of both size intervals visually fit the CLOUD15 data set.

The difference in the positions of the measuring points might be explained by the installation of FLOTUS which took place during the CLOUD15 measurement campaign while the aim of CLOUD16T was to test and calibrate FLOTUS. Thus, it can be assumed that during these two measurement campaigns a large number of aged organic contaminants influenced the composition of the contents of the CLOUD chamber. In contrast, FLOTUS did not even exist during CLOUD12. A solution for that issue would be to concentrate more on the use of mass spectrometers to filter out the effects of unwanted organics.

It is also plausible to consider inadequate calibration of the measuring devices as a potential cause of the differences. This hypothesis seems to make

sense, particularly in respect of the time gap between the CLOUD12 and the subsequent campaigns.

5.3.3 Comparison of Volatility Classes

Figures 30 and 31 illustrate the growth rates versus a sum over all VBS-bins. Again the first Figure 30 shows GR interval [1.8-3.2] nm and the second Figure 31 interval [3.2-8.0] nm.

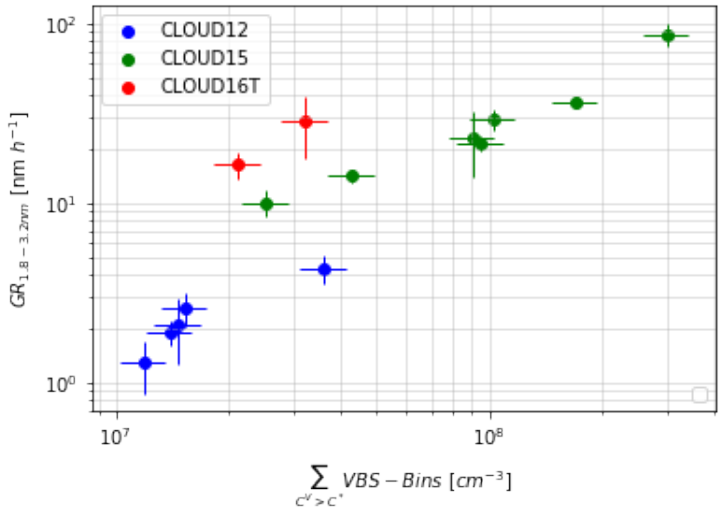

Figure 30: GRs vs. $\sum_{C^V>C^*}$ VBS-Bins in the interval [1.8-3.2] nm.

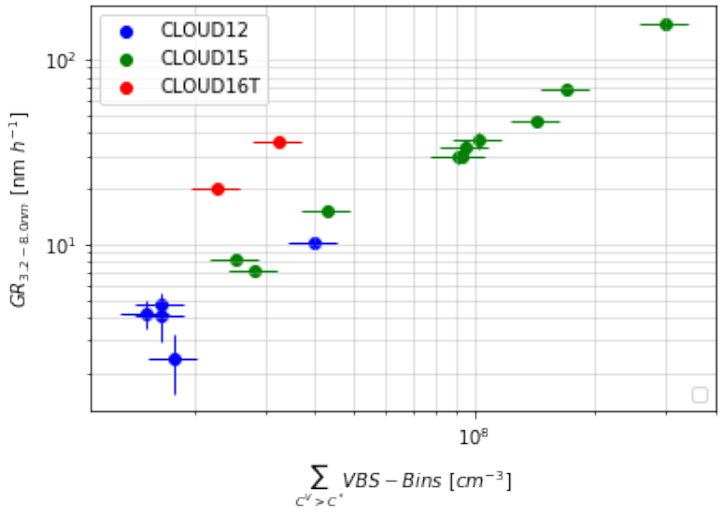

Figure 31: GRs vs. $\sum_{C^V>C^*}$ VBS-Bins in the interval [3.2-8.0] nm.

Since there was not enough data available to carry out a complete separation into VBS bins like in [6], the volatility classes ULVOC, ELVOC, and LVOC

were summed up for the CLOUD16T runs instead. The error in the concentrations of the volatility classes results here, like previously for the HOMs, from the measurement uncertainty of the CI-APi-TOF, given as 14 %.

Compared to the HOM plots, it can be observed here that the CLOUD16T measuring points in particular lie above the other measuring points. Differences bigger than a factor of 2 can be identified. The classification into VBS bins usually does not contain the whole range of ULVOC, ELVOC and LVOC. Therefore, taking into account the other summation, a higher concentration of the summed volatility classes would actually be expected. This trend may be caused by a different composition of the volatile organic substances in CLOUD16T. Despite an overall lower concentration, the volatility classes in CLOUD16T could be made up of more compounds that are relevant for particle growth. In other words the VOCs of CLOUD16T are for example made up of more ULVOCs than the compared campaigns. A better focus on mass spectroscopy would also provide more insight here.

Like the previous HOM comparison, inadequate calibration of the measuring devices can possibly be responsible for the differences between the measurement campaigns. Often different tuning settings lead to modified sensitivities, which are difficult to correct.

Regarding both HOM concentrations and volatility classes, an incorrect or different classification must also be considered as a possible cause for the differing results. The data provided to me was obtained directly from CERN and was also used in other evaluations and publications, which is why I do not assume the figures are incorrect.

5.4 Technical Issues during the CLOUD16T Campaign

The technical problems that occured during the CLOUD16T campaign concerning the DMA-train and may have influenced the measurements are also worth mentioning.

Right at the beginning of the experiment multiple issues with the Nano-Enhancer were encountered, causing the flow rate to drop significantly. The Nano-Enhancer was disassembled and a troubleshooting was carried out. Finally, a defective connection between the DEG-Fill and the reservoir was found. From this point onwards, the connection was plugged and the Nano-Enhancer was filled by hand, which worked surprisingly well.

Towards the end of the measurement campaign, a noticeable background noise occurred within the PSM CPC. After several attempts to drain the CPC and to dry the wick, it turned out that the Nano-Enhancer CPC combination was not connected to the chamber. The coupling was probably forgotten to be reconnected after maintenance.

Furthermore, the built-in HV source broke and had to be replaced with another one. As the new one only had six manually adjustable channels, switching between 6.2 nm and 8.0 nm channels had to be omitted. Therefore, it is absolutely necessary to equip the DMA-train with a suitable HV source before the next use.

Since the baseline measurements took place at the beginning of CLOUD16T, the results were very likely not influenced by the later problems. The workaround regarding the broken DEG connection should have worked well, no more problems have appeared again in this context. However, these issues should be kept in mind for further measurements.

6 | Conclusion and Outlook

The aim of this master thesis was to analyse the accuracy of the measurement methodology of the CERN CLOUD project by comparing baseline measurements of different CLOUD campaigns. For this purpose, the growth rates measured with the DMA-train during CLOUD16T were analysed and first compared with the same growth rates measured with NAIS. As a next step, the growth rates were plotted against different gas-phase variables and the trends of the data were compared with each other. These variables include the reaction rate of α-pinene ozonolysis during the growth rate measurement, the HOM signal in the nitrate CI-APi-TOF and the sum over several (low) volatility classes.

The first results indicate that the instruments agree fairly well. There is no significant difference between particle size distributions measured using the DMA-train and those obtained with the NAIS. The measured GRs are located close to the x=y line (if uncertainties taken into account, even on the line) and confirm previously published findings.

The ozonlysis reaction rates indicate that the growth rates of all measurement campaigns behave exponentially and in agreement with published expectations. Concerning the HOM concentrations during particle growth, especially CLOUD12 is remarkable. CLOUD12 took place before FLOTUS started. Therefore the CLOUD chamber might have been polluted during CLOUD15 and CLOUD16T by aged organics produced by FLOTUS, which were not counted by the mass spectrometers. However, the VOC comparisons demonstrate a variation of the growth rates taken from CLOUD16T. Approaches

to explain these discrepancies are a different composition of the volatile organic compounds. Furthermore, the calibration of the instruments should not be neglected. The time periods between the campaigns might be quite long and the functionality of the instruments changes over time due to operational stress.

To summarize, a general agreement in growth rates between the DMA-train and NAIS, as well as a reasonable overlap with previous campaigns, was identified. However, some issues were also detected. Nevertheless, future CLOUD campaigns should definitely take the influence of FLOTUS and aged organics into account. For a more accurate analysis more baseline measurements would be necessary. The inclusion of different temperatures analogous to publication [6] would also be an option to gain more information. It would be interesting to see whether the shapes of the diagrams differ notably at other temperatures. Another aspect to improve the measurement methodology would be the implementation of new methods to calculate particle growth rates. An example would be the 'maximum concentration method' presented in [14].

Finally, the importance of aerosol and environmental research should be underlined once again. CLOUD contributes significantly in this field and an accurate measurement methodology is therefore indispensable.

List of Figures

List of Tables

Bibliography

[1] William C. Hinds. *Aerosol Technology : Properties, Behavior, and Measurement of Airborne Particles*. 1999.

[2] Thomas F. Stocker, Dahe Qin, Gian Kasper Plattner, Melinda M. B. Tignor, Simon K. Allen, Judith Boschung, Alexander Nauels, Yu Xia, Vincent Bex, and Pauline M. Midgley. *Climate Change 2013 – The Physical Science Basis: Working Group I Contribution to the Fifth Assessment Report of the Intergovernmental Panel on Climate Change*. 2014.

[3] Jim Haywood. *Chapter 27 - Atmospheric Aerosols and Their Role in Climate Change*. 2016.

[4] Eri Saikawa, Vaishali Naik, Larry W. Horowitz, Junfeng Liu, and Denise L. Mauzerall. Present and potential future contributions of sulfate, black and organic carbon aerosols from china to global air quality, premature mortality and radiative forcing. *Atmospheric environment (1994)*, 43:2814–2822, 2009.

[5] Robert Wagner, Chao Yan, Katrianne Lehtipalo, Jonathan Duplissy, Tuomo Nieminen, Juha Kangasluoma, Lauri R. Ahonen, Lubna Dada, Jenni Kontkanen, Hanna E. Manninen, Antonio Dias, Antonio Amorim, Paulus S. Bauer, Anton Bergen, Anne-Kathrin Bernhammer, Federico Bianchi, Sophia Brilke, Stephany Buenrostro Mazon, Xuemeng Chen, Danielle C. Draper, Lukas Fischer, Carla Frege, Claudia Fuchs, Olga Garmash, Hamish Gordon, Jani Hakala, Liine Heikkinen, Martin Heinritzi, Victoria Hofbauer, Christopher R. Hoyle, Jasper Kirkby, Andreas Kürten, Alexander N. Kvashnin, Tiia Laurila, Michael J. Lawler, Huajun Mai, Vladimir Makhmutov, Roy Mauldin, Ugo Molteni, Leonid Nichman, Wei

Nie, Andrea Ojdanic, Antti Onnela, Felix Piel, Lauriane L. J. Quéléver, Matti P. Rissanen, Nina Sarnela, Simon Schallhart, Kamalika Sengupta, Mario Simon, Dominik Stolzenburg, Yuri Stozhkov, Jasmin Tröstl, Yrjö Viisanen, Alexander L. Vogel, Andrea C. Wagner, Mao Xiao, Penglin Ye, Urs Baltensperger, Joachim Curtius, Neil M. Donahue, Richard C. Flagan, Martin Gallagher, Armin Hansel, James N. Smith, António Tomé, Paul M. Winkler, Douglas Worsnop, Mikael Ehn, Mikko Sipilä, Veli-Matti Kerminen, Tuukka Petäjä, and Markku Kulmala. The role of ions in new particle formation in the cloud chamber. *Atmospheric chemistry and physics*, 17:15181–15197, 2017.

[6] Dominik Stolzenburg et al. Rapid growth of organic aerosol nanoparticles over a wide tropospheric temperature range. *PNAS*, 115:9122–9127, 2018.

[7] Dominik Stolzenburg. *How clusters grow to particles: Particle size distribution and growth rate measurements with a DMA-train*. PhD thesis, 2018.

[8] Markku Kulmala, Veli-Matti Kerminen, Tatu Anttila, Ari Laaksonen, and Colin D. O'Dowd. Organic aerosol formation via sulphate cluster activation. *Journal of Geophysical Research: Atmospheres*, 109, 2004.

[9] Hamish Gordon, Jasper Kirkby, Urs Baltensperger, Federico Bianchi, Martin Breitenlechner, Joachim Curtius, Antonio Dias, Josef Dommen, Neil M. Donahue, Eimear M. Dunne, Jonathan Duplissy, Sebastian Ehrhart, Richard C. Flagan, Carla Frege, Claudia Fuchs, Armin Hansel, Christopher R. Hoyle, Markku Kulmala, Andreas Kuerten, Katrianne Lehtipalo, Vladimir Makhmutov, Ugo Molteni, Matti P. Rissanen, Yuri Stozkhov, Jasmin Trostl, Georgios Tsagkogeorgas, Robert Wagner, Christina Williamson, Daniela Wimmer, Paul M. Winkler, Chao Yan, and Ken S. Carslaw. Causes and importance of new particle formation in the present-day and preindustrial atmospheres. *Journal of geophysical research. Atmospheres*, 122:8739–8760, 2017.

[10] R. Wagner, C. Yan, K. Lehtipalo, J. Duplissy, T. Nieminen, J. Kangasluoma, L. R. Ahonen, L. Dada, J. Kontkanen, H. E. Manninen, A. Dias, A. Amorim, P. S. Bauer, A. Bergen, A.-K. Bernhammer, F. Bianchi, S. Brilke, S. B. Mazon, X. Chen, D. C. Draper, L. Fischer, C. Frege, C. Fuchs, O. Garmash, H. Gordon, J. Hakala, L. Heikkinen, M. Heinritzi, V. Hofbauer, C. R. Hoyle, J. Kirkby, A. Kürten, A. N. Kvashnin, T. Laurila, M. J. Lawler, H. Mai, V. Makhmutov, R. L. Mauldin III, U. Molteni, L. Nichman, W. Nie, A. Ojdanic, A. Onnela, F. Piel, L. L. J. Quéléver, M. P. Rissanen, N. Sarnela, S. Schallhart, K. Sengupta, M. Simon, D. Stolzenburg, Y. Stozhkov, J. Tröstl, Y. Viisanen, A. L. Vogel, A. C. Wagner, M. Xiao, P. Ye, U. Baltensperger, J. Curtius, N. M. Donahue, R. C. Flagan, M. Gallagher, A. Hansel, J. N. Smith, A. Tomé, P. M. Winkler, D. Worsnop, M. Ehn, M. Sipilä, V.-M. Kerminen, T. Petäjä, and M. Kulmala. The role of ions in new particle formation in the cloud chamber. *Atmospheric Chemistry and Physics*, 17:15181–15197, 2017.

[11] Ian Colbeck and Mihalis Lazaridis. *Aerosol Science: Technology and Applications*. 2014.

[12] Jasmin Tröstl, Wayne K Chuang, Hamish Gordon, Martin Heinritzi, Chao Yan, Ugo Molteni, Lars Ahlm, Carla Frege, Federico Bianchi, Robert Wagner, Mario Simon, Katrianne Lehtipalo, Christina Williamson, Jill S Craven, Jonathan Duplissy, Alexey Adamov, Joao Almeida, Anne-Kathrin Bernhammer, Martin Breitenlechner, Sophia Brilke, Antònio Dias, Sebastian Ehrhart, Richard C Flagan, Alessandro Franchin, Claudia Fuchs, Roberto Guida, Martin Gysel, Armin Hansel, Christopher R Hoyle, Tuija Jokinen, Heikki Junninen, Juha Kangasluoma, Helmi Keskinen, Jaeseok Kim, Manuel Krapf, Andreas Kürten, Ari Laaksonen, Michael Lawler, Markus Leiminger, Serge Mathot, Ottmar Möhler, Tuomo Nieminen, Antti Onnela, Tuukka Petäjä, Felix M Piel, Pasi Miettinen, Matti P Rissanen, Linda Rondo, Nina Sarnela, Siegfried Schobesberger, Kamalika Sengupta, Mikko Sipilä, James N Smith, Gerhard Steiner, Antònio Tomè, Annele Virtanen, Andrea C Wagner, Ernest Weingartner, Daniela

Wimmer, Paul M Winkler, Penglin Ye, Kenneth S Carslaw, Joachim Curtius, Josef Dommen, Jasper Kirkby, Markku Kulmala, Ilona Riipinen, Douglas R Worsnop, Neil M Donahue, and Urs Baltensperger. The role of low-volatility organic compounds in initial particle growth in the atmosphere. *Nature (London)*, 533:527–531, 2016.

[13] John H Seinfeld. *Atmospheric chemistry and physics : from air pollution to climate change*. 2016.

[14] Lubna Dada, Katrianne Lehtipalo, Jenni Kontkanen, Tuomo Nieminen, Rima Baalbaki, Lauri Ahonen, Jonathan Duplissy, Chao Yan, Biwu Chu, Tuukka Petäjä, Kari Lehtinen, Veli Matti Kerminen, Markku Kulmala, and Juha Kangasluoma. Formation and growth of sub-3-nm aerosol particles in experimental chambers. *Nature Protocols*, 15:1013–1040, 2020.

[15] Jasper Kirkby. Cloud: A particle beam facility to investigate the influence of cosmic rays on clouds. pages 175–248, 2002.

[16] 2019-2021 progress report on ps215/cloud. https://cds.cern.ch/record/2783498/files/SPSC-SR-300.pdf, 2021. Last visit: 2024-08-12.

[17] J. Duplissy, M. B. Enghoff, K. L. Aplin, F. Arnold, H. Aufmhoff, M. Avngaard, U. Baltensperger, T. Bondo, R. Bingham, K. Carslaw, J. Curtius, A. David, B. Fastrup, S. Gagné, F. Hahn, R. G. Harrison, B. Kellett, J. Kirkby, M. Kulmala, L. Laakso, A. Laaksonen, E. Lillestol, M. Lockwood, J. Mäkelä, V. Makhmutov, N. D. Marsh, T. Nieminen, A. Onnela, E. Pedersen, J. O. P. Pedersen, J. Polny, U. Reichl, J. H. Seinfeld, M. Sipilä, Y. Stozhkov, F. Stratmann, H. Svensmark, J. Svensmark, R. Veenhof, B. Verheggen, Y. Viisanen, P. E. Wagner, G. Wehrle, E. Weingartner, H. Wex, M. Wilhelmsson, and P. M. Winkler. Results from the cern pilot cloud experiment. *Atmospheric chemistry and physics*, 10:1635–1647, 2010.

[18] Jasper Kirkby and CLOUD Collaboration. Atmospheric nucleation and growth in the CLOUD experiment at CERN. *AIP Conference Proceedings*, 1527:278–286, 2013.

[19] António Dias, Sebastian Ehrhart, Alexander Vogel, Christina Williamson, Joao Almeida, Jasper Kirkby, Serge Mathot, Samuel Mumford, and Antti Onnela. Temperature uniformity in the cern cloud chamber. *Atmospheric measurement techniques*, 10:5075–5088, 2017.

[20] Jasper Kirkby, António Amorim, Urs Baltensperger, Kenneth S. Carslaw, Theodoros Christoudias, Joachim Curtius, Neil M. Donahue, Imad El Haddad, Richard C. Flagan, Hamish Gordon, Armin Hansel, Hartwig Harder, Heikki Junninen, Markku Kulmala, Andreas Kürten, Ari Laaksonen, Katrianne Lehtipalo, Jos Lelieveld, Ottmar Möhler, Ilona Riipinen, Frank Stratmann, Antonio Tomé, Annele Virtanen, Rainer Volkamer, Paul M. Winkler, and Douglas R. Worsnop. Atmospheric new particle formation from the cern cloud experiment. *Nature geoscience*, 16:948–957, 2023.

[21] Eva Sommer and Pedro Rato. Flotus: a new addition to the cloud experiment. https://ep-news.web.cern.ch/content/flotus-new-addition-cloud-experiment, March 2023. Last visit: 2024-08-18.

[22] X. Y. Liu. Heterogeneous nucleation or homogeneous nucleation? *The Journal of chemical physics*, 112:9949–9955, 2000.

[23] Hanna Vehkamäki and Ilona Riipinen. Thermodynamics and kinetics of atmospheric aerosol particle formation and growth. *Chemical Society reviews*, 41:516–5173, 2012.

[24] Katrianne Lehtipalo, Jenni Kontkanen, Juha Kangasluoma, Alessandro Franchin, Daniela Wimmer, Siegfried Schobesberger, Heikki Junninen, Tuukka Petäjä, Mikko Sipilä, Douglas R. Worsnop, Markku Kulmala, Katrianne Lehtipalo, Jyri Mikkilä, Joonas Vanhanen, Johannes Leppä, and Douglas R. Worsnop. Methods for determining particle size distribution

and growth rates between 1 and 3 nm using the particle size magnifier. *Boreal environment research*, 19:215–236, 2014.

[25] Federico Bianchi, Theo Kurten, Matthieu Riva, Claudia Mohr, Matti P Rissanen, Pontus Roldin, Torsten Berndt, John D Crounse, Paul O Wennberg, Thomas F Mentel, Jurgen Wildt, Heikki Junninen, Tuija Jokinen, Markku Kulmala, Douglas R Worsnop, Joel A Thornton, Neil Donahue, Henrik G Kjaergaard, and Mikael Ehn. Highly oxygenated organic molecules (hom) from gas-phase autoxidation involving peroxy radicals: A key contributor to atmospheric aerosol. *Chemical reviews*, 119:3472–3509, 2019.

[26] Richard M Felder. *Elementary principles of chemical processes*. 1978.

[27] N. M. Donahue, S. A. Epstein, S. N. Pandis, and A. L. Robinson. A two-dimensional volatility basis set: 1. organic-aerosol mixing thermodynamics. *Atmospheric chemistry and physics*, 11:3303–3318, 2011.

[28] L. Poulain, A. Tilgner, M. Brüggemann, P. Mettke, L. He, J. Anders, O. Böge, A. Mutzel, and H. Herrmann. Particle-phase uptake and chemistry of highly oxygenated organic molecules (homs) from -pinene oh oxidation. *Journal of Geophysical Research: Atmospheres*, 127, 2022.

[29] N. M Donahue, A. L Robinson, C. O Stanier, and S. N Pandis. Coupled partitioning, dilution, and chemical aging of semivolatile organics. *Environmental science technology*, 40:2635–2643, 2006.

[30] D. Stolzenburg, G. Steiner, and P. M. Winkler. A dma-train for precision measurement of sub-10 nm aerosol dynamics. *Atmospheric Measurement Techniques*, 10:1639–1651, 2017.

[31] Peter Kallinger, Gerhard Steiner, and Wladyslaw W. Szymanski. Characterization of four different bipolar charging devices for nanoparticle charge conditioning. *Journal of nanoparticle research : an interdisciplinary forum for nanoscale science and technology*, 14, 2012.

[32] Athanasios Mamakos. Methodology to quantify the ratio of multiple-to single-charged fractions acquired in aerosol neutralizers. *Aerosol Science and Technology*, 50:363–372, 2016.

[33] TSI. Tsi advanced aerosol neutralizer model 3088. https://tsi.com/getmedia/85d6abad-a56a-4a1f-a61d-1c73983c7e7a/Aerosol2022. Last visit: 2024-08-18.

[34] Pramod Kulkarni, Paul A Baron, and Klaus Willeke. *Aerosol measurement: principles, techniques, and applications*. 2011.

[35] Sophia Brilke. *Sub-10 nm aerosol nanoparticle characterization : from mobility standards to ambient new particle formation*. PhD thesis, 2020.

[36] Richard C. Flagan. Electrical mobility methods for submicrometer particle characterization. pages 339–364, 2011.

[37] Gerhard Steiner. *High resolution mobility spectrometry of molecular ions and their effect on the charging probabilities of airborne particles under bipolar diffusion charging conditions*. PhD thesis, 2011.

[38] D. Wimmer G. Steiner, M. Attoui and G. P. Reischl. A medium flow, high-resolution vienna dma running in recirculating mode. *Aerosol Science and Technology*, 44(4):308–315, 2010.

[39] J. Kangasluoma, L. Ahonen, M. Attoui, H. Vuollekoski, M. Kulmala, and T. Petäjä. Sub-3 nm particle detection with commercial tsi 3772 and airmodus a20 fine condensation particle counters. *Aerosol science and technology*, 49:674–681, 2015.

[40] TSI Incorporated. *ULTRAFINE CONDENSATION PARTICLE COUNTER MODEL 3776 - OPERATION AND SERVICE MANUAL*, 2014.

[41] 2021 Airmodus Ltd. *nano Condensation Nucleus Counter system MODEL A11 nCNC USER MANUAL*, 2021.

[42] TSI Incorporated. *NANO ENHANCER MODEL 3777 - OPERATION AND SERVICE MANUAL*, 2016.

[43] Hanna E. Manninen, Sander Mirme, Aadu Mirme, Tuukka Petäjä, and Markku Kulmala. How to reliably detect molecular clusters and nucleation mode particles with neutral cluster and air ion spectrometer (nais). *Atmospheric measurement techniques*, 9:3577–3605, 2016.

[44] S. Mirme and A. Mirme. The mathematical principles and design of the nais - a spectrometer for the measurement of cluster ion and nanometer aerosol size distributions. *Atmospheric measurement techniques*, 6:1061–1071, 2013.

[45] T. Jokinen, M. Sipilä, H. Junninen, M. Ehn, G. Lönn, J. Hakala, T. Petäjä, R. L. Mauldin, M. Kulmala, and D. R. Worsnop. Atmospheric sulphuric acid and neutral cluster measurements using ci-api-tof. *Atmospheric chemistry and physics*, 12:4117–4125, 2012.

[46] Goethe Universität Frankfurt am Main. Nitrate ci-api-tof. https://www.uni-frankfurt.de/65565070. Last visit: 2024-08-18.

[47] Paul Scherrer Institut PSI. Api-tof. https://www.psi.ch/en/lac/api-tof. Last visit: 2024-08-18.

[48] IONICON. Ptr3 the method, hardware and performance of the ptr3. https://www.ionicon.com/technologies/details/ptr3. Last visit: 2024-04-25.

[49] Martin Breitenlechner, Lukas Fischer, Markus Hainer, Martin Heinritzi, Joachim Curtius, and Armin Hansel. Ptr3: An instrument for studying the lifecycle of reactive organic carbon in the atmosphere. *Analytical chemistry (Washington)*, 89:5824–5831, 2017.

[50] Thermo Fisher Scientific Air Quality Instruments. *Model 49C Instruction Manual UV Photometric O3 Analyzer Part Number 9999*, 2007.

[51] M. Kulmala, L. Laakso, K. E. J. Lehtinen, I. Riipinen, M. Dal Maso, T. Anttila, V.-M. Kerminen, U. Hõrrak, M. Vana, and H. Tammet. Initial

steps of aerosol growth. *Atmospheric chemistry and physics*, 4:2553–2560, 2004.

[52] Victor G. Khamaganov and Ronald A. Hites. Rate constants for the gas-phase reactions of ozone with isoprene, - and -pinene, and limonene as a function of temperature. *The Journal of Physical Chemistry A*, 105:815–822, 2001.

[53] C N Hewitt, S Hayward, and A Tani. The application of proton transfer reaction-mass spectrometry (ptr-ms) to the monitoring and analysis of volatile organic compounds in the atmosphere. *Journal of environmental monitoring*, 5:1–7, 2003.

[54] Mario Simon, Martin Heinritzi, Stephan Herzog, Markus Leiminger, Federico Bianchi, Arnaud Praplan, Josef Dommen, Joachim Curtius, and Andreas Kurten. Detection of dimethylamine in the low pptv range using nitrate chemical ionization atmospheric pressure interface time-of-flight (ci-api-tof) mass spectrometry. *Atmospheric measurement techniques*, 9:2135–2145, 2016.